The Dissertation Committee for Xin Zheng Certifies that this is the approved version of the following dissertation:

Schrödinger Equation Monte Carlo Simulation of Nanoscale Devices

Committee:

Leonard F. Register, Supervisor

Sanjay K. Banerjee

Jack C. Lee

Allan H. MacDonald

Matthew J. Gilbert

Schrödinger Equation Monte Carlo Simulation of Nanoscale Devices

by

Xin Zheng, B.S., M.S.E.

Dissertation

Presented to the Faculty of the Graduate School of

The University of Texas at Austin

in Partial Fulfillment

of the Requirements

for the Degree of

Doctor of Philosophy

The University of Texas at Austin

December 2007

Dedication

Dedicated to my loving parents and wife

Acknowledgements

This work would not have been possible without the generous support of many others. I am greatly indebted to my advisor Dr. Leonard Franklin Register for his support and guidance throughout the course of this work. His advice and support have made my graduate research an enjoyable and rewarding experience. I would also like to thank Dr. Banerjee for the advice and guidance. Special thanks also go to Dr. Lee, Dr. MacDonald and Dr. Gilbert for serving my committee.

I am grateful to my fellow co-workers for their help and collaboration. Special thanks to Wanqiang Chen, Kengming Liu, Xiaofeng Fan and Ningyu Shi who have directly or indirectly contributed towards this research. In addition I would like to thank Di Li, Geng Wang, Yang Chen, Yueran Liu, Fei Li, Li Lin, Ning Kong and many others for their friendship and help.

Last, but certainly not least, I would like to thank my wife, Hui, and my parents for their abiding love, encouragement, and support.

Schrödinger Equation Monte Carlo Simulation of Nanoscale Devices

Publication No._____________

Xin Zheng, Ph.D.
The University of Texas at Austin, 2007

Supervisor: Leonard F. Register

Some semiconductor devices such as lasers have long had critical dimensions on the nanoscale where quantum effects are critical. Others such as MOSFETs are now being scaled to within this regime. Quantum effects neglected in semiclassical models become increasing important at the nanoscale. Meanwhile, scattering remains important even in MOSFETs of 10 nm and below. Therefore, accurate quantum transport simulators with scattering are needed to explore the essential device physics at the nanoscale. The work of this dissertation is aimed at developing accurate quantum transport simulation tools for deep submicron device modeling, as well as utilizing these simulation tools to study the quantum transport and scattering effects in the nano-scale semiconductor devices.

The basic quantum transport method "Schrödinger Equation Monte Carlo" (SEMC) provides a physically rigorous treatment of quantum transport and phase-breaking inelastic scattering (in 3D) *via real (actual) scattering processes such as optical*

and acoustic phonon scattering. The SEMC method has been used previously to simulate carrier transport in nano-scaled devices in order to gauge the potential reliability of semiclassical models, phase-coherent quantum transport, and other limiting models as the transition from classical to quantum transport is approached. In this work, SEMC-1D and SEMC-2D versions with long range polar optical scattering processes have been developed and used to simulate quantum transport in tunnel injection lasers and nano-scaled III-V MOSFETs. Simulation results serve not only to demonstrate the capabilities of the developed quantum transport simulators, but also to illuminate the importance of physically accurate simulation of scattering for the predictive modeling of transport in nano-scaled devices.

Table of Contents

CHAPTER 1. INTRODUCTION

The concept of scaling has been consistently applied to the modern semiconductor industry over many technology generations to consistently improve both the package density and device performance [1]. The International Roadmap for Semiconductors (ITRS) [2] suggests that the gate length of CMOS will be scaled down below 10 nm by the end of the next decade. Critical dimensions including the channel length have or will approach and fall below the carrier phase coherence length and thermal DeBroglie wavelength. Therefore quantum mechanical effects that were neglected in the semi-classical transport models will need to be considered carefully, particularly in unconventional MOSFET structures such as SOI, FinFETS and vertical channel MOSFETs, and perhaps including Si-Ge-C heterostructures. As drift-diffusion, hydrodynamic, and semi-classical Monte Carlo simulator have been used before, accurate quantum transport simulators will be needed to explore the essential device physics that cannot be readily explored via experiments, and as a design tool for developing new devices.

Several different approaches [3-5] have been proposed to study the quantum transport in ultra-small devices. Each of the different approaches has its advantages and disadvantages. Among them, the non-equilibrium Green's function technique "<u>S</u>chrödinger <u>E</u>quation <u>M</u>onte <u>C</u>arlo" (SEMC) [6] addresses the transition from quantum to semiclassical transport by solving the Schrödinger equation for a model coupled carrier-phonon many-body system, so that phase-breaking with respect to the carrier due to inelastic scattering *occurs* within SEMC just as it occurs within the true coupled carrier-phonon system, via the change of the phonon coordinate. Thus SEMC is a good candidate for studying the quantum transport phenomenon, especially in the regime that the transition from semiclassical to quantum mechanical transport happens. (Quasi) one-dimensional (1D) versions of SEMC have been successfully applied to study essential quantum transport physics in devices such as quantum well lasers [7, 8] and MOSFETs [9], and a two-dimensional version has been developed to model elstrostatically self-consistent transport in nanoscale MOSFET structures [10, 11].

The following chapters are organized as follows:

Chapter 2 is provided as background. A description of SEMC method is provided with descriptions borrowed with permission from papers by my advisor Dr. Register [6], and a prior graduate and postdoctoral student, Wanqiang Chen [12].

Chapter 3, the first part is the injection and scattering in a tunnel injection laser structure in the presence of coupling to bulk phonon modes [8]. My part in work is setting up an appropriated device and calculating the device parameters via bound-state calculations prior to running SEMC can run on this device. This work demonstrates breakdown of Golden Rule based scattering calculations.

Next part is the transport and scattering in quantum cascade lasers. This work was began by replacing the model bulk phonon modes with the confined and interface polar optical phonon modes of the heterostructure system for more realistic modeling of scattering, optical phonon mediated depopulation of intermediate states being an essential mechanism of operation for these devices [13]. The calculation of these modes by transfer matrix method and the implementation of these modes into SEMC is the first challenge of this work. Then SEMC was applied to simulate transport and scattering in a model quantum cascade laser, obtain results again not available via a Golden Rule treatment of scattering and, under some circumstances, in contradiction to expectations of a Golden Rule treatment of scattering [14].

Chapter 4 considers transport and scattering in Si-based MOSFET structure. The study is looking at specific effects of quantum-mechanical non-locality *along* the channel on thermal velocity and drive current in the ballistic limits as channels shrinks toward and below 10 nm in length [15]. It should be noted that this work was required to allow isolation of the effects of quantum-mechanical non-locality *along* the channel on scattering, for which SEMC provides unique capabilities and to which I have only recently begun study as discussed above. However, these limiting results are, nevertheless, of interest in themselves.

Chapter 5 discusses the non-local scattering effects along the channel in nanoscale CMOS. In self-consistent calculations of scattering, the carrier's scattering rate (or perhaps more accurately, its imaginary self energy) as a function of position is affected not just by the quantum nature of the initial state but by the quantum mechanical density of final states. For non-randomizing processes, the degree of quantum mechanical non-locality can become more pronounced as we know from past work [6]. For Si-based MOSFETs surface-roughness scattering is such a source of non-randomizing scattering.

Chapter 6 gives summary and future work recommendations. Typically the most promising III-V MOSFETs. III-V materials such as GaAs, InSb have much higher electron mobilities and, thus, offer improved device performance [16-18], although the reduced density of states in these devices can be counterproductive. Also, bandgap engineering and direct bandgaps, not available in Si- and Ge-based material systems, allow for novel designs and make high performance integrated optoelectronic circuits combining MOS and photonic devices a possibility. However, with longer wavelengths, longer phase coherence lengths and scattering often dominated by the very non-randomizing non-polar optical phonon scattering process, consideration of quantum transport will be even more critical.

CHAPTER 2. SIMULATION METHOD: SEMC

2.1 THE CARRIER-PHONON SCHRÖDINGER EQUATION

As the dimensions of MOSFETs scale deep into the sub-0.1μm regime [2] and new materials such as SiGe(C) alloys are introduced in semiconductor devices [19], eventually semi-classical models of transport can be expected to become unreliable. So-called quantum transport simulators have been employed to extend our understanding of transport in nanoscale MOSFETs, but these methods typically have simple models of scattering if any. In contrast, the quantum transport simulator "Schrödinger Equation Monte Carlo" (SEMC) [6] provides physically rigorous treatment of quantum transport and phase-breaking inelastic scattering (in 3D) *via real (actual) scattering processes such as optical and acoustic phonon scattering.* In this section, a brief description of SEMC, the simulation tool I use in this work, is provided.

Schrödinger Equation Monte Carlo addresses the transition from quantum to semi-classical transport by solving the Schrödinger equation for a model coupled carrier-phonon many-body system, so that phase-breaking with respect to the carrier due to inelastic scattering *occurs* within SEMC just as it occurs within the true coupled carrier-phonon system, via the change of the phonon coordinate. A brief description of SEMC as used in this work follows; a more detailed description of SEMC and the translation from **r**-space to x and $\mathbf{k}_{y,z}$-space for the quasi-one-dimensional simulations of this work are provided within [6] and references therein.

Consider a charge carrier within a semiconductor coupled to the various approximately harmonic vibrational modes of the crystal lattice. The evolution of the coupled system, in principle, could be described without further approximation via the multi-particle Schrödinger Equation [20],

$$\begin{gathered} i\hbar \frac{\partial}{\partial t}\psi(r, n_1,\ldots, n_q,\ldots, n_Q) = (H_c + H_{OS})\psi(r, n_1,\ldots, n_q,\ldots, n_Q) + \\ \sum_{\pm}\sum_{q=1}^{Q}(\frac{\hbar}{2\omega_q})^{1/2} M(r, q)\sqrt{nq + \frac{1}{2} \pm \frac{1}{2}}\psi(r, n_1,\ldots, n_q + 1,\ldots, n_Q) \end{gathered} \tag{2.1}$$

Here $\psi(r, n_1,\ldots,n_q,\ldots,n_Q)$ is the carrier-oscillator wave function in terms of the (three-dimensional) carrier real-space coordinate r and the oscillator eigenfunction quantum numbers n_q , where q labels the classical (but not necessarily plane-wave) oscillator modes. The Hamiltonian $H_c(r)=T(r)+V(r)$ operates only on the carrier coordinate, where T and V are the carrier kinetic energy operator and potential energy functions, respectively. (T is taken to be a function of carrier position to allow for a spatially vary effective mass.) The operator, $H_{os}=\sum_{q=1}^{Q}\hbar\omega_q(n_q + \frac{1}{2})$, operates only on the oscillator coordinates, where the $\hbar\omega_q$ are the characteristic energy separations for the harmonic oscillator eigenstates, i.e., the phonon energies. The last term on the right-hand-side of Eq.(2.1) allows scattering between "nearest-neighbor" oscillator eigenstates due to the carrier-oscillator coupling, that is phonon emission or absorption, where the $M(r, q)$ are the coupling potentials. With respect to the carrier, this latter term represents its self-energy, both real and imaginary components, due to coupling to the phonon system.

The coupling of the carrier to the oscillator/phonon degrees of freedom in Eq.(2.1) produces phase breaking inelastic scattering with respect to the carrier even though, in fact, energy is conserved and coherence maintained throughout the full carrier-oscillator Q+ dimensional space. To obtain some observable property of the carrier, the observable is calculated in each phonon state independently and then the results summed, as opposed to summing the wave functions over the phonon states and then calculating the observable. Since the contributions from different states do not add coherently, there is the appearance of phase breaking. To conserve overall energy in the full multi-particle system, the change in oscillator energy associated with the scattering from one phonon state $\{n_1,...,n_q,...,n_Q\}$ to another $\{n_1,...,n_q \pm 1,...,n_Q\}$ must be accompanied by a change in energy of $\mp\hbar\omega_q$ associated with the carrier. Further, each time the carrier-phonon system scatters from one state to another, it is then coupled to 2Q-1 new states(phonon emission and absorption), where Q is on the order of Avogadro's number, in addition to the old state. Thus (neglecting virtual processes for the moment) the multi-particle wave function continues to branch out into new states with each phonon emission or absorption in an essentially irreversible process.

2.2 THE BASIC (COORDINATE SYSTEM INDEPENDENT) SEMC METHOD

Direct numerical solution of a Schrödinger Equation with roughly Avogadro's number of degree of freedom is not possible. However, the above discussion demonstrates the essential physics of phase breaking inelastic scattering of carriers, and that phase breaking inelastic scattering of carriers obviously can be treated within a Hamiltonian system so long as additional degrees of freedom are provided. The challenge is to design a model carrier-phonon system that is both of manageable size and accurately mimics the true carrier-phonon system, at least with respect to the propagation of the carrier.

To achieve manageable size, rigorous modeling of scattering is restricted to first-order scattering processes, both real and virtual. As a result only the initial oscillator state $\{n_1,...,n_{q'},...,n_{Q'}\}$ and its 2*Q'* nearest-neighbor final states $\{n_1,...,n_{q'} \pm 1,...,n_{Q'}\}$ must be considered simultaneously, along with model probability sources and sinks, as diagramed in Figure 2.1. In most semiconductors such an approximation is well justified. For example, in GaAs the second order term produces well under a one-percent correction to the band edge hole self-energy due to carrier-polar-optical phonon coupling; for electrons the correction is less than a tenth of a percent [21]. Thus, for the model system:

$$\begin{aligned} E\psi_i(\boldsymbol{r},n_1,...,n_q,...,n_Q) &= [H_c(\boldsymbol{r})+H_{s,i}(\boldsymbol{r})]\psi_i(\boldsymbol{r},n_1,...,n_q,...,n_Q) \\ &+\sum_{\pm}\sum_{q=1}^{Q}(\frac{\hbar}{2\omega_q})^{\frac{1}{2}}M(\mathrm{r},q)\sqrt{n_q+\frac{1}{2}\pm\frac{1}{2}}\psi_f(\boldsymbol{r},n_1,...,n_q\pm 1,...,n_Q)+\Omega(\boldsymbol{r}) \end{aligned} \tag{2.2}$$

for the initial state, $\psi(r,n_1,...,n_{q'},...,n_{Q'}) \rightarrow \psi_i(r)$, and

$$\begin{aligned} (E\mp\hbar\omega)\psi_f(\mathbf{r},n_1,...,n_q\pm 1,...,n_Q) &= [H_c(\mathbf{r})+H_{s,f}(\mathbf{r})]\psi_f(\mathbf{r},n_1,...,n_q\pm 1,...,n_Q) \\ &+(\frac{\hbar}{2\omega_q})^{\frac{1}{2}}M(\mathbf{r},q)\sqrt{n_q+\frac{1}{2}\pm\frac{1}{2}}\psi_i(\mathbf{r},n_1,...,n_q,...,n_Q) \end{aligned} \tag{2.3}$$

for the 2*Q'* final states, $\psi(r,n_1,...,n_{q'}\pm 1,...,n_{Q'}) \rightarrow \psi_f(r,q',\pm)$ for emission and absorption, respectively, where $H_c(\boldsymbol{r})$ is the Hamiltonian for the carrier alone. The term $\Omega(r)$ represents source such as a boundary source or scattering into the "initial" state from a previous state. The operators H_s are probability sinks such as absorbing boundaries on the simulation region and/or complex potentials representing subsequent scattering in the final states, i.e., the final-state self-energies of the carrier. These complex potentials allow higher order scattering effects such as collisional broadening to be modeled, and in the absence of an absorbing boundary such as for bound QW states, provide a necessary outlet for probability current from the final state. For convenience, the zero-point energy reference has been chosen as that of the initial uncoupled oscillator state so that only the changes in the oscillator energy with scattering need to be tracked. If the number of model phonon modes *Q*’ can be reduced to matter of perhaps hundreds, then the problem of solving a Schrödinger Equation is reduced to a manageable problem of self-consistency solving 2*Q*’+1~100 coupled Schrödinger’s in the carrier coordinate only.

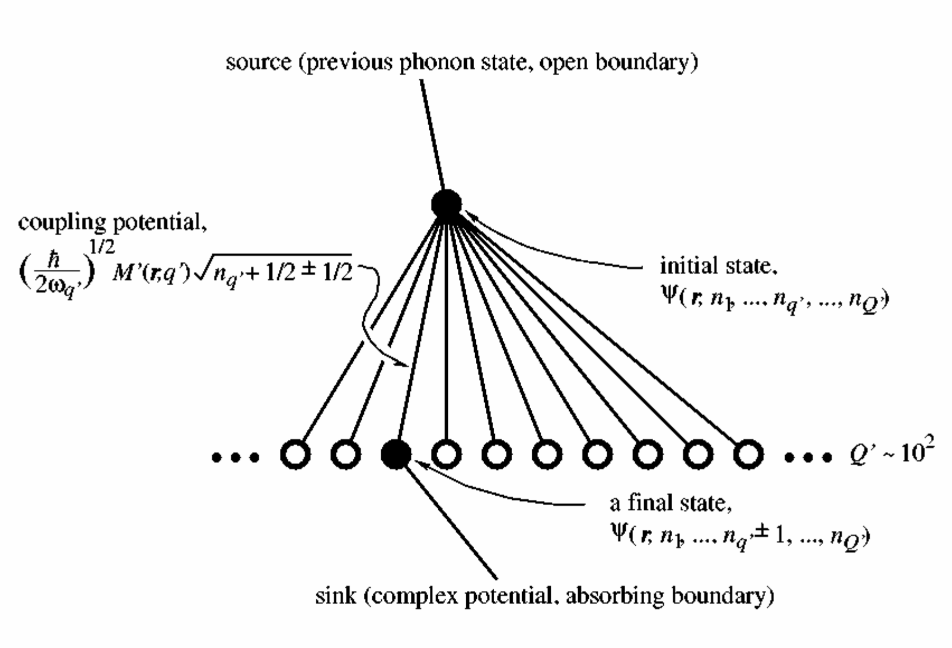

Figure 2.1: Schematic representation of the many-body carrier-phonon system within the phonon coordinate space. $n_1, n_2, \ldots n_Q$ showing the initial and the many final nearest neighbor phonon states and their coupling potentials. As indicated, the wave functions and coupling potentials are also functions of the carrier coordinate r.

In principle, there is also a question of having to average simulation results over many initial phonon states $\{n_1, \ldots, n_{q'}, \ldots, n_{Q'}\}$ subject to the occupation probabilities for each oscillator state $n_{q'}$ for each mode *q*’. However, the strength of all first order processes simply varies linearly with the value $n_{q'}$, i.e., as $n_{q'} + \frac{1}{2} \pm \frac{1}{2}$ for real and virtual phonon emission or absorption, respectively. Therefore, the expectation values of the $n_{q'}$ can be use directly in Eqs. (2.2) and (2.3) to obtain the correct expected first-order scattering probabilities, even though the expectation values of the $n_{q'}$ are in general non-integer valued. Thus, only one initial phonon "state", although with non-integer values of the $n_{q'}$, need be considered.

To achieve accuracy, meaning both to mimic first order scattering in the much large true system and avoid high-order (backscattering) artifacts of a small system [22], with such a limited number of phonon modes requires both using model coupling potentials characteristic of the true carrier-phonon system and effectively spreading coupling among the model phonon modes, and to do so without a priori knowledge of which true phonon mode contributes significantly to scattering. SEMC achieves this goal via a Monte Carlo technique that samples the model coupling potentials from those of the true system. However, the model coupling potentials are not simply sampled directly from among those of the true system; rather, the model coupling potentials are generated such that each has on average the spatial correlation function characteristic of the sum of the true coupling potentials for phonons of approximately the same energy. That is, such that

$$Q'\langle M'(r,q')M'(s,q')\rangle = \sum_{q=1}^{Q} M(r,q)M(s,q) \tag{2.4}$$

where the "$\langle\ \rangle$" terms indicate the expectation value. (Ion displacements from equilibrium and thus, the coupling potentials, are inherently real quantities so that there is no need to distinguish their complex or Hermitian conjugates). A random-phase superposition of the true coupling potentials is the most straight forward, and physically clear, method of creating the SEMC coupling potentials to satisfy Eq. (2.4). However, any method of generating the model coupling potentials that accomplishes this task can be used.

Although the true phonon modes are not used, providing the model system phonon modes with the spatial correlation function characteristic of the phonon modes of the true system on average, results in the same first order scattering on average; the correlation function of Eq. (2.4) is an element of any first-order scattering calculation for carriers. As an illustrative example, consider a Fermi's Golden Rule calculation of the transition probability between an initial carrier state $\psi_i(r)$ and a final state $\psi_f(r)$ due to optical phonon scattering:

$$\begin{aligned}\left\langle S'(\psi_i,\psi_f)\right\rangle &= \int d^3r\int d^3s\,\psi_f{}^*(r)\psi_f(s)Q'\left\langle M'(r,q')M'(s,q')\right\rangle\psi_i(r)\psi_i{}^*(s)\\ &\times\frac{\pi}{\omega_{op}}(n_{\omega_{op}}+\frac{1}{2}\pm\frac{1}{2})\delta(E_f\pm\hbar\omega_{op}-E_i)\\ &= \int d^3r\int d^3s\,\psi_f{}^*(r)\psi_f(s)\left[\sum_{q=1}^{Q}M(r,q)M(s,q)\right]\psi_i(r)\psi_i{}^*(s)\\ &\times\frac{\pi}{\omega_{op}}(n_{\omega_{op}}+\frac{1}{2}\pm\frac{1}{2})\delta(E_f\pm\hbar\omega_{op}-E_i)\\ &= S(\psi_i,\psi_f)\end{aligned}\tag{2.5}$$

where the "*i*" and "*f*" subscripts indicate the initial and final carrier states, *E* the carriers' initial energy, and $\hbar\omega_{op}$ the nearly constant optical phonon energy. Another way to see this point is to observe that to the extent that the true phonon modes are degenerate, any linear combination of those modes also is a valid true phonon mode.

The generation of each SEMC coupling potential consistent with Eq. (2.4) also effectively spreads the coupling among the model modes. Consider the case of bulk semiconductor material with plane-wave uncoupled carrier eigenstates and phonon modes. Even with collisional broadening, energy and momentum conservation requirements ensure that only small minority of the true phonon modes contribute significantly to the total scattering. In contrast, the noisy coupling potentials of SEMC are much more likely to contribute to scattering because each represents a superposition of many of the true modes. Thus, a statistically significant sample set of phonon modes can be achieved and high-order artifacts avoided with only a limited number of phonon modes.

This process then can be repeated to sample the carrier trajectory through an unlimited number of scattering “events”/phonon states as it continues to propagate in position r, much like semi-classical Monte Carlo except that scattering is neither local in position nor time, as illustrated in Fig 2.2. The old now known “initial” state becomes a probability source. A new “initial” state is selected stochastically from among the old “final” states according to the previously calculated probability current into each from the old “initial” state. A new set of “final” states and corresponding coupling potentials are generated to replace the old complex self-energy in the old “final state”. Still subsequent scattering is again represented by complex self-energies in the new “final” states. The new set of equations is then solved self-consistently to (re)obtain the new “initial” state, just as before.

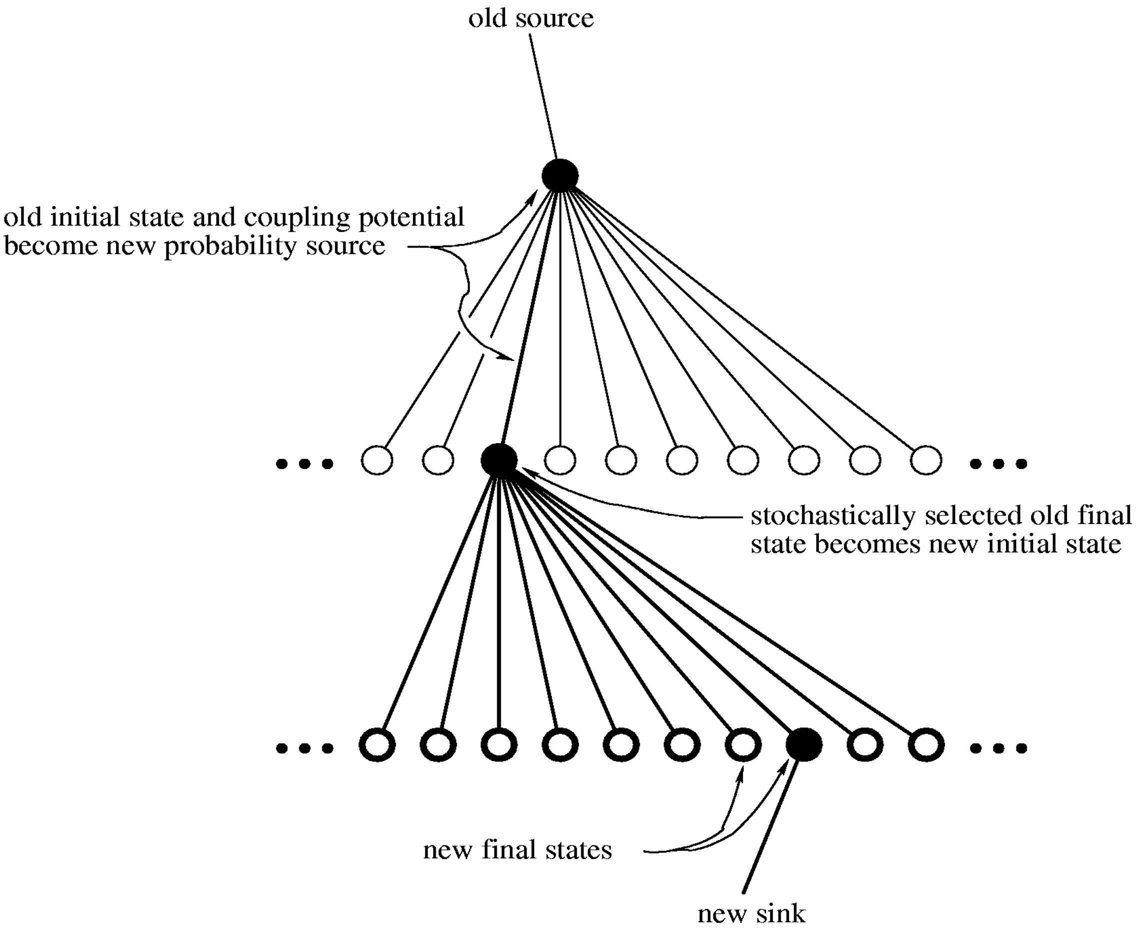

Figure 2.2: This figure shows the sequential scattering in SEMC. The old initial state and coupling potential becomes the new probability source, a new initial state is selected stochastically from the old final states, and new set of final states is generated, each with its own sink.

To summarize the basic SEMC algorithm for modeling carrier transport with phase breaking inelastic scattering:

I: A model carrier-phonon system is defined with a limited number of phonon modes and only the initial and nearest-neighbor final states of the phonon system are considered.

II: coupling potentials are generated consistent with Eq. (2.4).

III: The set of Schrödinger Equations, Eq. (2.2), and Eq. (2.3), are then solved self-consistency for the carrier-phonon wave-function of the model system, a non-perturbative approach that inherently conserves probability.

IV: All observable such as carrier position, probability current and energy then can be obtained directly from the carrier-phonon wave function of the model system. In this way first-order scattering in the true system can be mimicked with quantitative accuracy in the model SEMC system.

CHAPTER 3. QUANTUM WELL LASERS

3.1 INTRODUCTION

In conventional quantum well lasers, in principle, the time required for capture electrons to reach low energy states of the lasing subband via dissipative phonon interactions can be comparable to or larger than the lifetime of the carriers within the lasing subband prior to recombination, resulting in a hot electron distribution within the quantum wells [23]. Hot electron distribution, in turn, lead to gain suppression, reduced quantum efficiency, and increased diffusion capacitance, greater low-frequency roll-off and high-frequency chirp [23-25]. Recently, “tunnel injection lasers” have been developed to minimize electron heating within the active quantum well region by direct injection of cool electrons from the separate confinement region into the lasing subband(s) through a tunneling barrier.

Tunnel injection lasers, however, also present a rich physics of transport and scattering, and a correspondingly rich set of challenges to simulation and device optimization. The quantum well region is designed such that the lasing subbands of the quantum well are nominally degenerated and, thus, delocalized among the wells. A Golden-Rule (GR) based analysis of the carrier injection in to the active region, which by design is phonon assisted, would suggest an approximately uniform injection of the electrons into any number of quantum wells. However, such an analysis overlooks (in part, via a random-phase approximation among the final states) the basic real-space transport requirement that injected carriers still must pass through the wells sequentially, coherently or otherwise, with an associated attenuation of the injected current into each subsequent well due to electron-hoe recombination in the prior well. The required transport among the wells then can be either thermionic, or, of theoretically increasing importance for low temperature carriers, phonon-assisted or coherent tunneling. Coherent resonant tunneling between wells, however, is sensitive to even small potential drops that split the energies of the lasing subbands and localizes the electron states to individual wells.

In this chapter these issues are addressed using SEMC based quantum transport simulation. SEMC provides a qualitatively and quantitatively accurate, non-perturbative, current conserving treatment of coherent transport and incoherent/phonon-mediated transport due to real scattering processes, including the dominant process of long-range polar-optical phonon scattering, and already has been used to study the effects of phase-coherence and phase-breaking on carrier capture by quantum wells [7].

3.2 MODEL TUNNEL INJECTION LASER BY APPLICATION OF BULK PHONON SCATTERING

3.2.1 Device Structure

The design objective of the tunnel injection laser is to deliver, in particular, “cool” electron uniformly among multiple quantum wells for recombination with holes. The goal of this work is to study the essential physics of this process within a quantum transport formalism, and compare the results with the expectations from simpler approaches. To this end, the quantum well/barrier structure to be simulated has been simplified by reducing the number of wells to one leading well and one following well, between which disparities in the carrier densities and capture rates and the reasons for those disparities may be more readily identified. Two structures are considered, modeled after discussed in [23], as defined in Table 3.1. Both of these structures are designed to have nominally degenerate ground state energies in the two wells 39meV below the conduction band edge of the electron injection side of the separate confinement region (Figure 3.1). The only significant difference between the two structures is the height of the barrier between the two wells; one equal to the height of the band edge on the hole injection side of the separate confinement region, the other equals to the height of the band edge on the electron injection side of the separate confinement region. Polar optical phonon scattering due to GaAs bulk modes was considered within the active region in this work. Consideration of the full spectrum of interface and confined phonon modes [26] will be addressed in the next section.

A	Sep. cont. GaAs	Tunnel barrier AlAs	Leading well InGaAs	Barrier GaAs	Trailing well InGaAs	*Sep. cont. GaAs*
Width (nm)	N/A	3	7	7	7	*N/A*
E_c (eV)	0	1.0	-0.117	0.1	-0.1	0.1
m^*/m_e	0.067	0.14	0.047	0.071	0.047	0.071
γ(non para. const.) (1/eV)	0.61	0.25	1.02	0.57	1.02	0.57

B	Sep. cont. GaAs	Tunnel barrier AlAs	Leading well InGaAs	Barrier GaAs	Trailing well InGaAs	Sep. cont. GaAs
Width (nm)	N/A	3	7	7	7	N/A
E_c (eV)	0	1.0	0	0	-0.1	0.1
m^*/m_e	0.067	0.14	0.047	0.067	0.047	0.071
γ (non para. const.) (1/eV)	0.61	0.25	1.02	0.61	1.02	0.57

Table 3.1: Well/barrier width w, conduction band edge E_c, effective mass in units of m_e, and nonparabalicity for model tunnel injection laser system with (A) high and (B) low interwell potential barriers.

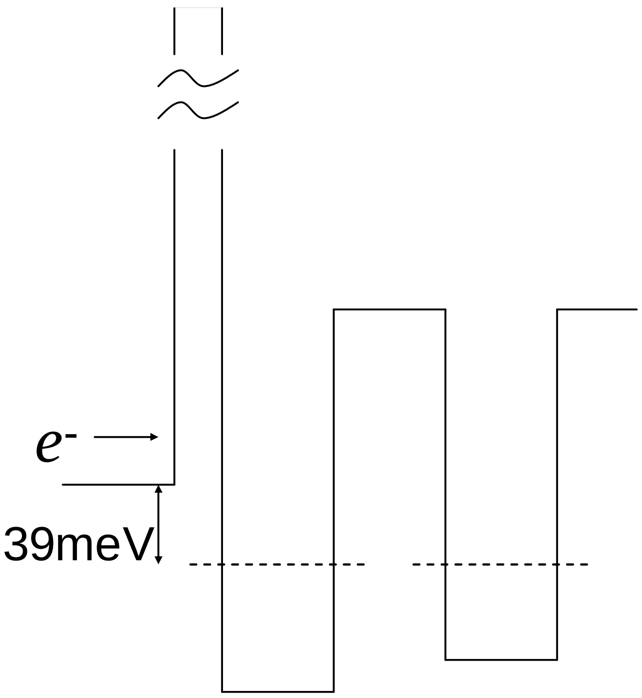

Figure 3.1: Schematic view of the high barrier structure. Note that the bound state is approximately one phonon energy below the well.

3.2.2 Simulation Results and Discussion

As noted above, a Golden-Rule based analysis would suggest uniform injection of electrons into the ground states of the two wells from low-energy incident electrons. However, as shown in Figure 3.2, there is a decided segregation of the charge after the initial capture/scattering event toward the leading well, and a significant fraction of the charge captured in the second well enters hot from higher energy incident electrons into the excited state of that well. Those electrons that are found in the ground state of the second well at low energies after one scattering event get there by tunneling from the first well after the scattering event, as shown in Figure 3.3.

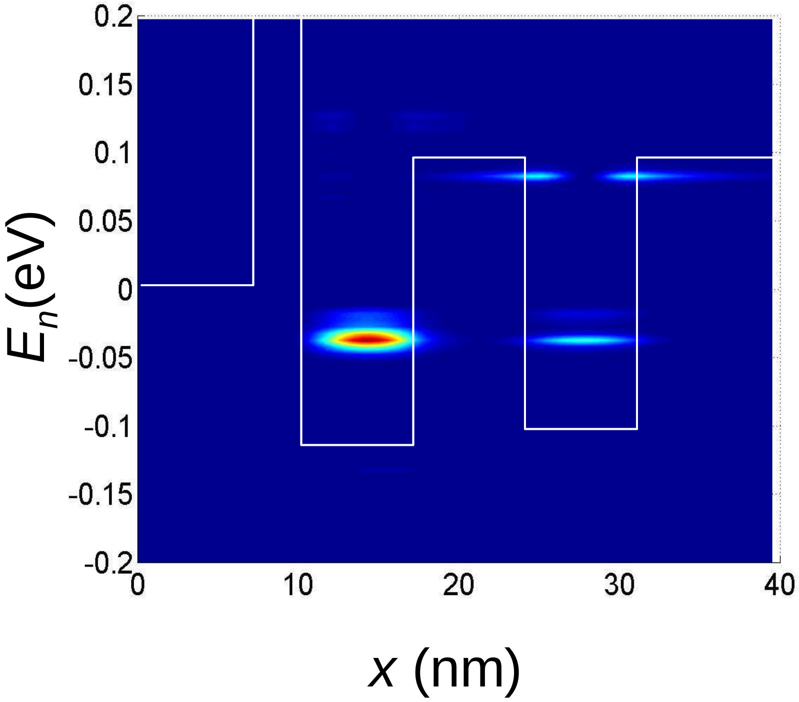

Figure 3.2: Carrier distributions (probability density) after first scattering event as a function of position and normal component of energy for a distribution of electrons incident from the left, with the conduction band edge shown for reference.

Over time, the inter-well tunneling will reduce but not eliminate this segregation, as shown in Figure 3.4(a). However, if a small additional voltage bias is applied, 26mV across the active region for this work, the resonant tunneling process is greatly attenuated resulting in further segregation of the carriers toward the leading well, as shown in Figure 3.4(b).

Reducing the barrier height for the second structure eliminates much of this problem, however, by allowing penetration of the incident carrier wave functions all of the way across the active region, leading to a nearly uniform distribution of electrons between the two wells after the initial capture process (and subsequently) at flatband, as shown in Figure 3.5(a), or under additional bias, as shown in Figure 3.5(b). We note that in these simulations, incident electrons enter the low barrier system with energy significantly above the barrier height as seen in Figure 3.6. However this result is a likely artifact of the scale of the system − there is a high energy resonant state in the active region; for larger, more realistic numbers of wells, low energy quasi-confined states should exist within the active region of the low barrier system to tunnel into.

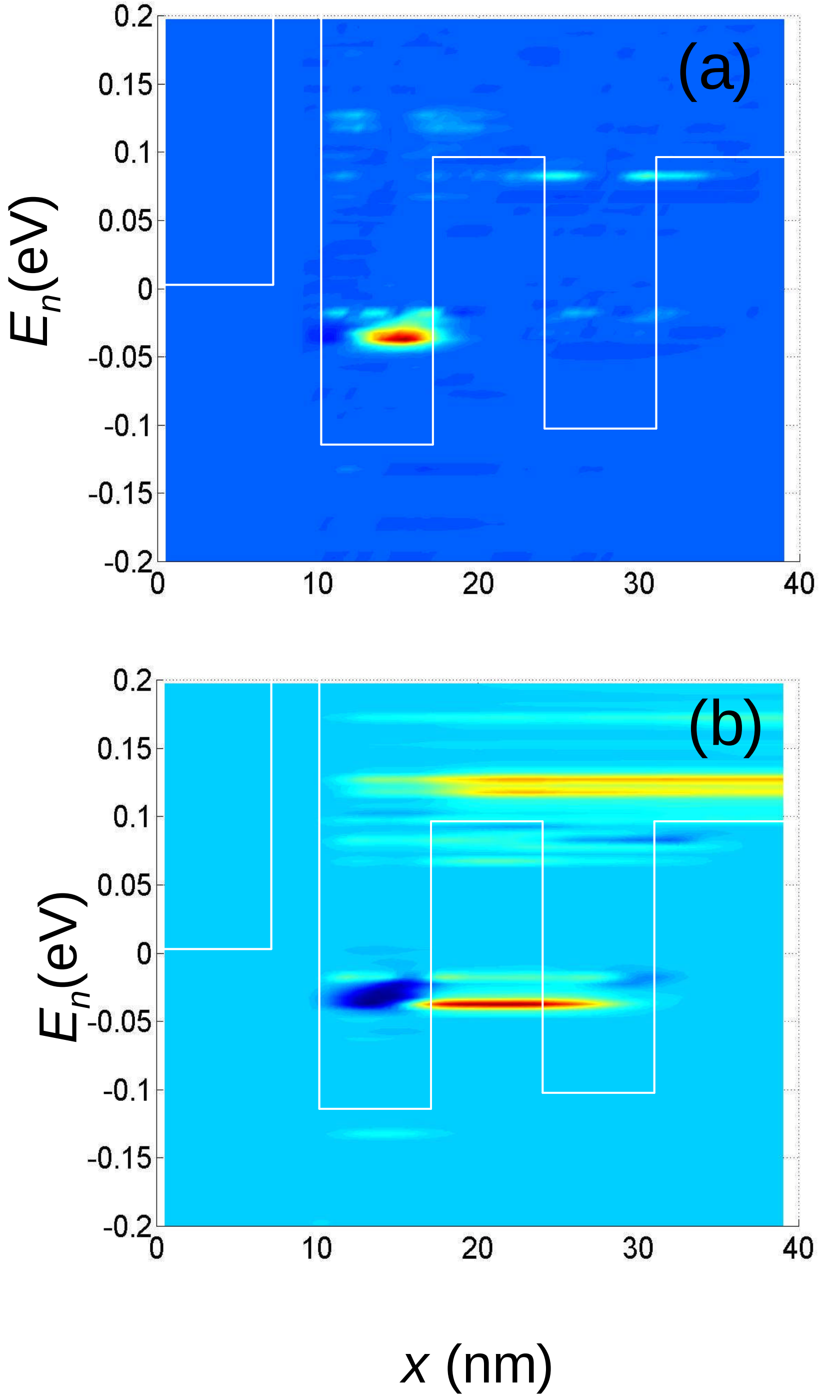

Figure 3.3: (a) The current flow, which is localized primarily to the leading well, from the initial/incident electron state to the final/captured electron states (in "phonon-space" as a function of the position and normal component of energy of the captured electrons. (b) The subsequent resonant real-space tunneling current from the first well to the second.

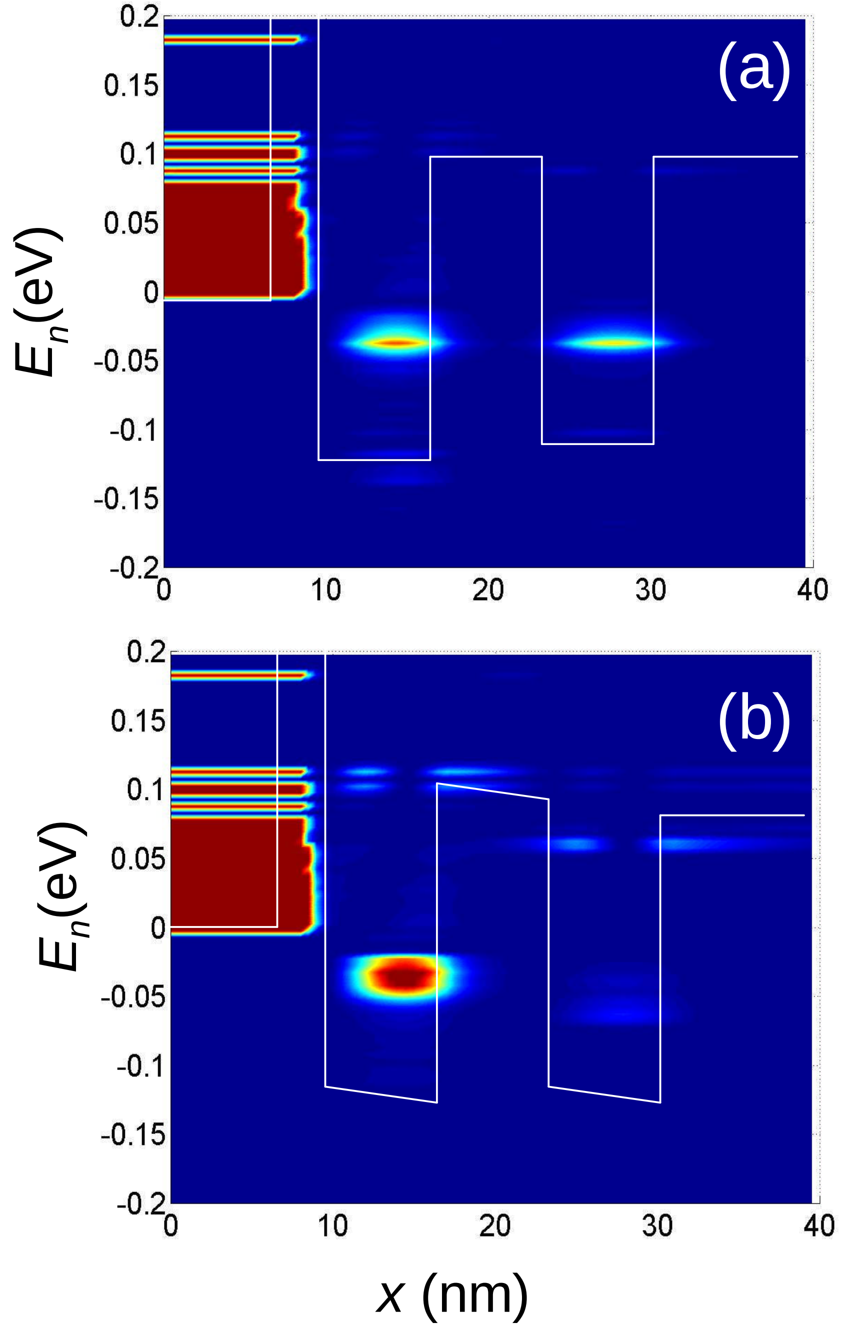

Figure 3.4: The cumulative probability densities within the wells through 10 scattering events as a function of position and normal component of energy (a) at flatband and (b) under additional bias.

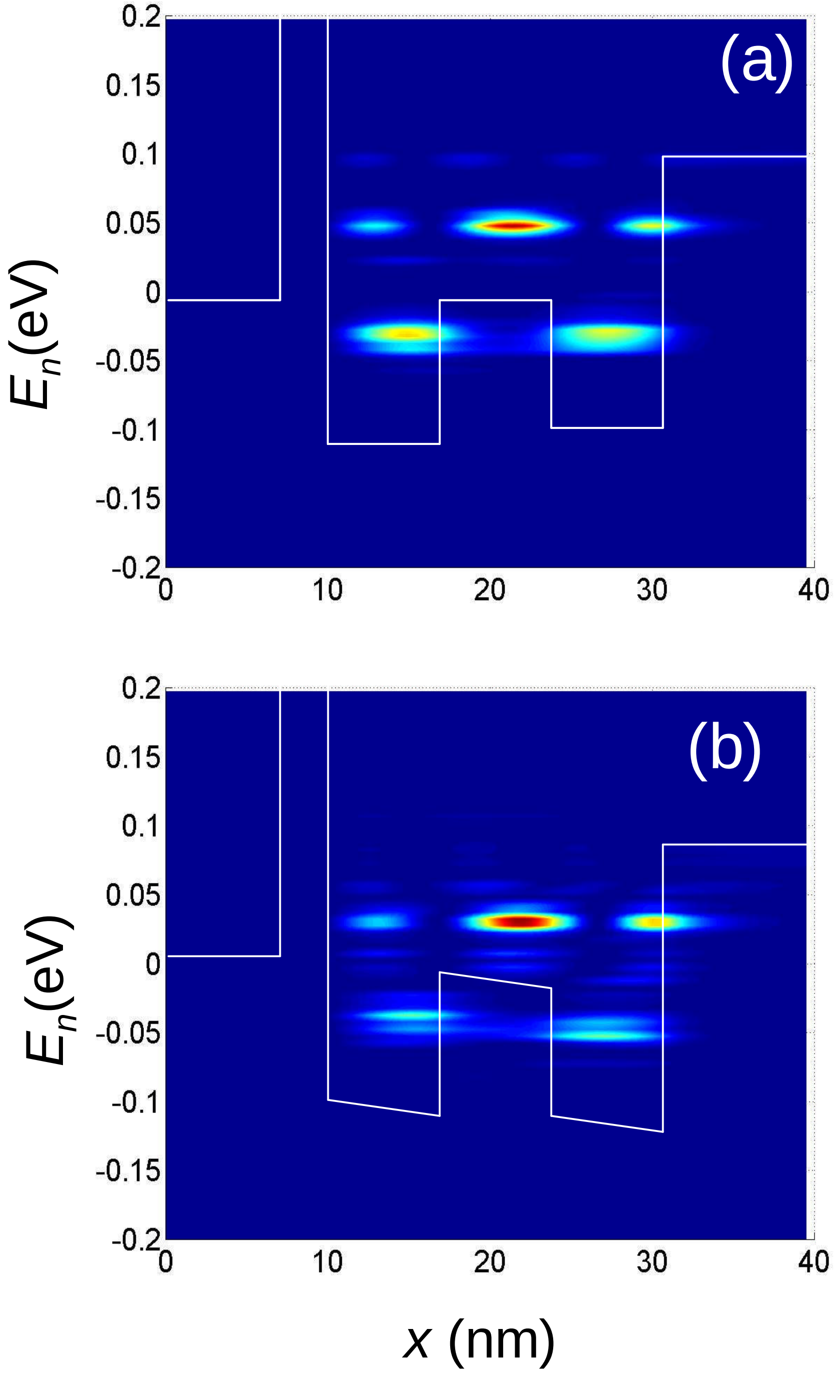

Figure 3.5: Carrier distribution (probability density) after the first scattering event as a function of position and well normal component of energy (a) at flatband , and (b) under additional bias (26mV across active region).

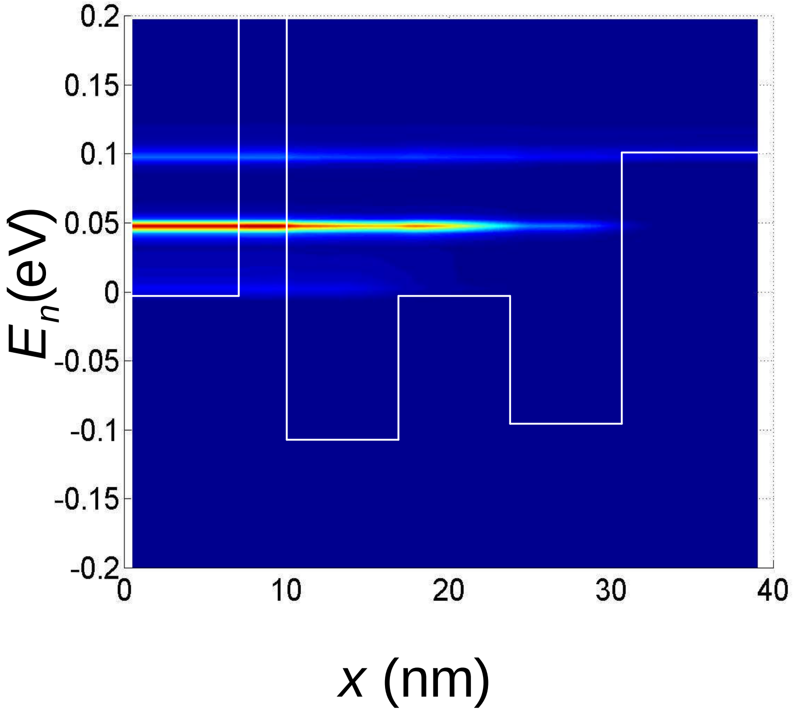

Figure 3.6: Real-space current flows into the active region as a function of position and normal component of energy.

In one regard, both system performed well (at least for a two well system) but particularly the low barrier system. As also seen in Figure 3.6, the fraction of carriers that leak beyond the well − resulting in diffusion capacitance and dark current − is quite low because of the offset between the conduction band-edge in the separate confinement region on the electron injection side and that on the hole injection side. Similarly, the tunnel barrier to electron injection should minimize hole transport beyond the active region that can be more significant than for electron transport as a result of the thermionic emission between wells. Further, the tunneling barrier may serve to allow hot electrons injected from the cladding layer more time to cool within the separate confinement region before entering the active region. The cost of the barrier, however, greatly reduced electron capture efficiency.

3.2.3 Conclusions

A study of transport in tunnel injection laser has been performed. It has been demonstrated that injection lasers can offer advantage over more conventional lasers by, as intended, lowering the carrier injection energy and by, in addition, reducing leakage currents. However, it has also been demonstrated that a Golden-Rule (GR) analysis of capture can be misleading, and that interwell transport may be quite sensitive to the voltage drops between wells. In order to make direct comparisons with experiments, comprehensive modeling should address these effects − although not necessarily requiring as rigorous as transport approach once the essential physics has been identified − and others. For example, although designed with electron transport in mind, these system also offer advantages for hole transport as suggest above. In addition the richer energy spectrum of the full set of phonon modes [26] as compared to that of a single mode used in this preliminary work may effect and perhaps enhance carrier capture and interwell transport [26]. I will address this issue in the following section.

3.3 MODELING OF INTERSUBAND (MONOPOLAR) INJECTION LASERS INCLUDING APPLICATION CONSIDERATION OF THE FULL PHONON SPECTRUM.

3.3.1 Phonon mode calculation

Optical phonon assisted electron transitions play an important role in heterotructure optical devices including intersubband lasers and tunnel-injection lasers [27-30] since preferential intersubband transition rates are critical to establish and maintain the population inversion for the device operation. In these structures, the intersubband electron transitions induce by electron-phonon interactions are the dominant relaxation process when the intersubband separation between the lasing states is made close to longitudinal-optical phonon energy.

It is well known that the shape and energies of optical phonon modes are modified by quantum wells. The presence of heterointerfaces gives rise to the confinement of LO phonons as well as localized phonons at the interfaces [26, 31-34]. This confinement also alters and splits the phonon energies. They can be calculated to a reasonable approximation based on the dielectric continuum model [31, 32]. Suppose an arbitrary multi-interface hetero-structure with interfaces at

$z_i, i = 1,2,...n.$

The dispersion relations and electrostatic potentials of the optical phonon modes and electron-phonon interaction Hamiltonians are obtained based on the dielectric continuum model and microscopic analysis; the interface phonon modes are calculated using the transfer matrix method.

Similar to electron confinement in the low-dimensional structures, both acoustic and optical phonons are modified in quantum well structures. In this work, I am mainly interested in the modified optical phonons because their energies are comparable to the desired intersubband separations. These phonon modes are the interface optical phonon modes, confined LO phonon modes, confined TO phonon modes, and half space LO and TO modes. While the confined and half space modes can be regarded as bulk modes “segmented” by the heterostructure interfaces, the interface modes are a new type of phonon with localized polarization and potential at the interfaces. These phonon modes can be calculated based on the dielectric continuum model and the microscopic analysis by Lucas et al [31] and Licari et al [32].

The electrostatic equations are:

$$\nabla \cdot D(r) = \rho_0(\mathrm{r})$$

$$D(r) = \varepsilon \cdot E(r) = \varepsilon_0 \cdot E(r) + P(r)$$

$$\varepsilon(\frac{\partial^2}{\partial z^2} - q^2)\phi(r) = 0$$

$$E(r) = -\nabla\varphi(r)$$

Where *E(r), D(r), P(r)* and *φ(r)* are the electric field, electric displacement, electric polarization and scalar potential, ε and ε_0 are dielectric constants of the respective materials and the permittivity of free space, respectively, and *ρ0* is the free charge density. Considering free oscillation with free charge density $\rho_0(r) = 0$, the above equations lead to

$$\varepsilon\nabla^2\phi(r) = 0$$

In a quantum well structure, since the system has no constraint on the *x-y* plane, we can write

$$\phi(r) = \frac{1}{\sqrt{A}} e^{iq\cdot p}\phi(z)$$

Where *A* is the in-plane cross section area of the structure, *q* and *p* are the two-dimensional in-plane wave vector and position vector, respectively. This gives

$$\varepsilon(\frac{\partial^2}{\partial z^2} - q^2)\phi(r) = 0$$

where *q* is the magnitude of the two-dimensional phonon in plane wave vector.

In a quantum well structure, the equation above is satisfied when $\varepsilon = 0$ or

$$(\frac{\partial^2}{\partial z^2} - q^2)\phi(r) = 0$$

with $\varepsilon = 0$, φ can be any function as long as the boundary conditions on *E(r)* and *D(r)* at the interface are satisfied.

For the structure shown above, $\varepsilon = 0$ leads to the following functional forms of the confined and half space LO modes. The frequencies of these modes are determined by setting $\varepsilon = 0$ and therefore are equal to the bulk LO mode frequencies.

For the confined phonon modes in region

$z \in (z_i, z_{i+1})$

We have

$$\phi(z) \propto \left\{ \begin{array}{ll} \cos\frac{m\pi}{z_{i+1} - z_i}(z - \frac{z_i + z_{i+1}}{2}), \quad m = 1,3,5,... & \\ & z_{\mathrm{i}} < z \le z_{i+1} \\ \sin\frac{m\pi}{z_{i+1} - z_i}(z - \frac{z_i + z_{i+1}}{2}), \quad m = 2,4,6,... & \end{array} \right\}$$

For the half space LO modes in regions

$z \in (-\infty, z_1) \cup (z_n, \infty)$

We have

$$\phi(z) \propto \left\{ \begin{array}{l} \sin\frac{2m\pi}{L}(z - z_1), \quad m = 1,2,3,... \ z \le -z_1 \\ \sin\frac{2m\pi}{L}(z - z_n), \quad m = 1,2,3,... \ z \ge z_n \end{array} \right\}$$

where *L* is the length of the half-space.

The interface phonon modes can be obtained when $\varepsilon \neq 0$, then the solution for

$$(\frac{\partial^2}{\partial z^2} - q^2)\phi(r) = 0$$

is a linear combination of exponential term, i.e.,

$$\phi_i(q,z) = c_{i-}e^{-qz} + c_{i+}e^{+qz}$$

Where "*i*" denotes the region label and C_i's are coefficients to be determined. The boundary conditions are

$$\phi_1(q,-L/2)=0$$
$$\phi_i(q,z_i)=\phi_{i-1}(q,z_i)$$
$$\varepsilon_i\frac{\partial}{\partial z}\phi_i(q,z_i)=\varepsilon_{i-1}\frac{\partial}{\partial z}\phi_{i-1}(q,z_i)$$
$$\phi_3(q,L/2)=0$$

Where z_i is the location of the *i*th interface. With these boundary conditions, the coefficients are determined up to a constant. Use matrix notation, the contents are related to as:

$$M_i(z_i)C_i=M_{i-1}(z_i)C_{i-1}$$

where the matrices C_i, M_i are given by

$$C_i=\begin{pmatrix}C_{i-}\\ C_{i+}\end{pmatrix}$$
$$M_i(z)=\begin{pmatrix}\phi_{i-}(z) & \phi_{i+}(z)\\ \varepsilon_i\phi'_{i-}(z) & \varepsilon_i\phi'_{i+}(z)\end{pmatrix}$$

By applying the chain rule, the matrix C_i may be expressed as

$$C_i=Q_i(z_i)Q_{i-1}(z_{i-1})\cdots Q_1(z_1)C_0$$

Where the transfer matrix $Q_i(Z_i)$ is defined as

$$M_i(z_i)^{-1}M_{i-1}(z_i)$$

Then $C_{n+}=0$ and $C_{o-}=0$ (which are got from $\phi=0$ at the two ends) means

$$\left[Q_n(z_n,q,w)Q_{n-1}(z_{n-1},q,w)\cdots Q_1(z_1,q,w)\right]_{2,2}=0$$

Solving this matrix problem, we can get the dispersion relation as a function of *q*.

The macroscopic dielectric continuum model based on classical electrostatics involves relatively simple formulations. It gives the functional form of the interface modes, confined and half space LO modes, but it cannot give TO modes because TO modes do not produce macroscopic electric field and charge density. Fortunately the TO modes do not interact with electrons for the same reason and we can ignore them completely. However, to formulate the interaction Hamiltonians between electrons and the interface, confined modes and half space LO phonon modes, we also need the amplitudes of these modes. These amplitudes can be derived from the orthonormality and completeness conditions of the phonon eigenfunctions, which can only be formulated in the microscopic framework. Assuming the standard forms for the continuum expressions of the ionic force equation and the polarization of the polar medium, the normalization relation is derived from an appropriate generalization of the optical-phonon normalization condition and is given by

$$\frac{\hbar}{2\omega}=\sum_i \frac{\varepsilon_0}{2\omega}\cdot\frac{\partial\varepsilon_i(w)}{\partial\omega}\int_{R_i} dz\left(q^2\left|\phi_i(q,z)\right|^2+\left|\frac{\partial\phi_i(q,z)}{\partial z}\right|^2\right)$$

from which the amplitude of electric potential for different modes can be determined.

For the confined LO and half space modes in structure I use, we have the following results of the electrostatic potential. For the confined modes in region:

$$z\in\left(z_i, z_{i+1}\right)$$

$$\phi(z)=\left(\frac{\hbar}{\varepsilon_0}\cdot\frac{1}{\partial\varepsilon_i(\omega)/\partial\omega}\right)^{1/2}\cdot\left(\frac{1}{q^2+\left(\frac{m\pi}{z_{i+1}-z_i}\right)^2}\right)^{1/2}\cdot\left(\frac{2}{z_{i+1}-z_i}\right)^{1/2}$$

$$\cdot\begin{cases}\cos\frac{m\pi}{z_{i+1}-z_i}\left(z-\frac{z_{i+1}+z_i}{2}\right), m=1,3,5\cdots \\ \sin\frac{m\pi}{z_{i+1}-z_i}\left(z-\frac{z_{i+1}+z_i}{2}\right), m=2,4,6\cdots\end{cases} \quad z_{\mathrm{i}}<z\le z_{i+1}$$

For the half space LO modes in regions:

$$z \in (-\infty, z_1) \cup (z_n, \infty)$$

$$\phi(z) = \left(\frac{\hbar}{\varepsilon_0} \cdot \frac{1}{\partial \varepsilon_i(\omega)/\partial \omega} \right)^{1/2} \left(\frac{1}{q^2 + \left(\frac{m\pi}{L} \right)^2} \right)^{1/2} \left(\frac{2}{L} \right)^{1/2}$$

$$\cdot \begin{cases} \sin \frac{m\pi}{L}(z - z_1), & m = 1,2,3,\cdots \quad z \le z_1 \\ \sin \frac{m\pi}{L}(z - z_n), & m = 1,2,3,\cdots \quad z \ge z_n \end{cases}$$

Figure 3.7 shows examples of confined and half space phonon modes potentials for an arbitrary 3-well, 2-barrier heterojunction. Confined modes are localized within each junction and, thus, the potential is zero at every interface. Their derivatives don’t have to be continuous across the interface.

And the expressions for the interface modes are also obtained by using the matrix solution. One of the interface phonon modes in a three interface heterojunction is plotted in Figure 3.8. While all interface phonon modes are maximized at the interfaces, the total potential in the middle of the region between interfaces can be relatively high:

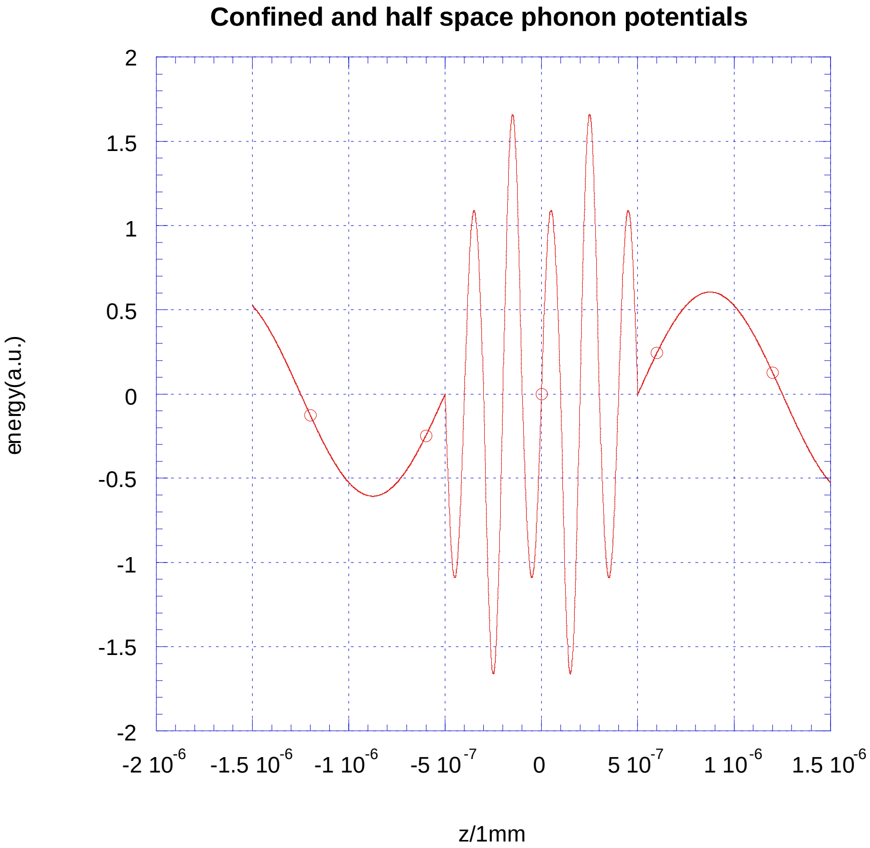

Figure 3.7: Examples of confined and half space phonon modes potentials for an arbitrary 3-well, 2-barrier heterojunction. Confined phonon modes: from *z* = -0.5nm to *z* = 0.5nm. Half-space phonon modes: *z* < -0.5nm and *z* > 0.5nm. For this plot, *qa* = 1, *m* = 2.

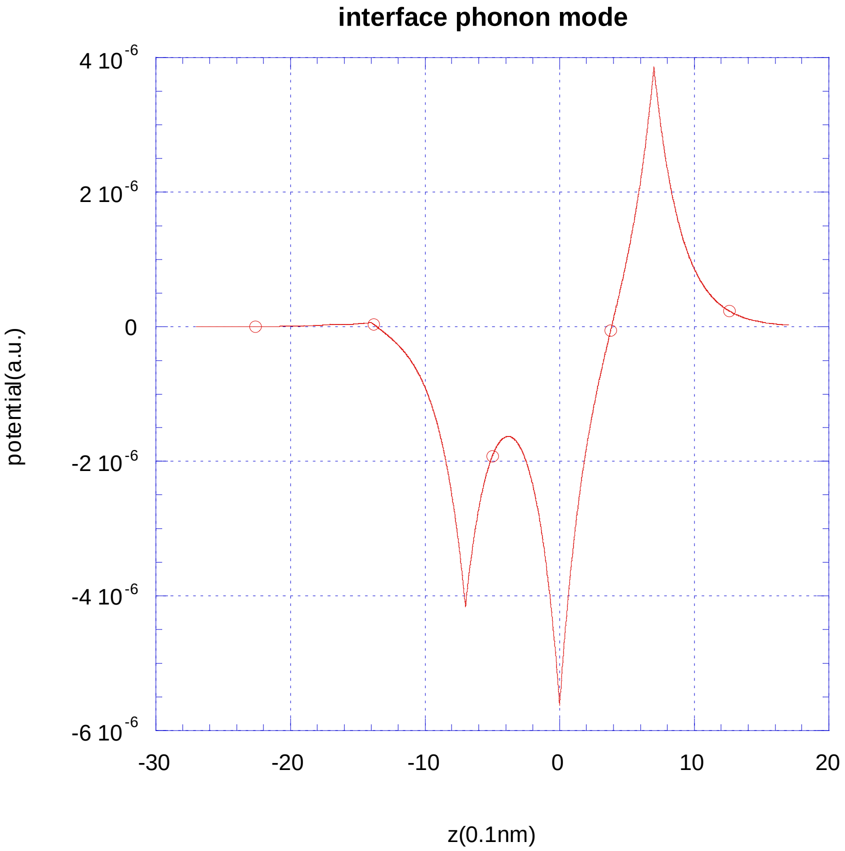

Figure 3.8: One of the interface phonon in a three interface heterojunction having interfaces at 0.7nm, 0nm, 0.7nm, respectively. For this plot, $qa = 1$.

3.3.2 Correlation function and coupling potential for phonon modes

In order to put phonon modes into the SEMC, we need their correlation function and coupling potential.

For confined phonon modes:

The correlation function is:

$$C\sum_{m=1}^{\infty}\frac{1}{q^2+\left(\frac{m\pi}{a}\right)^2}G_m(x_1)G_m(x_2)\equiv P$$

Where

$$C=\frac{\hbar}{\varepsilon_0}\cdot\frac{1}{\partial\varepsilon_i(\omega)/\partial\omega}\cdot\frac{2}{a}$$

$$G_m(x)=\begin{cases}\cos(\frac{m\pi x}{a}) & m=1,3,5...\\ \sin(\frac{m\pi x}{a}) & m=2,4,6...\end{cases}$$

The summation over m can be performed after some manipulation:

$$P=C\sum_{m=1}^{\infty}\frac{1}{q^2+\left(\frac{m\pi}{a}\right)^2}\left[\frac{1}{2}\cos(\frac{m\pi}{a}(x_1-x_2))-\frac{1}{2}(-)^m\cos(\frac{m\pi}{a}(x_1+x_2))\right]$$

$$=C\sum_{m=1}^{\infty}\frac{1}{q^2+\left(\frac{m\pi}{a}\right)^2}\cdot\frac{1}{2}\cos(\frac{m\pi}{a}(x_1-x_2))$$

$$-C\sum_{m=1}^{\infty}\frac{1}{q^2+\left(\frac{m\pi}{a}\right)^2}\cdot\frac{1}{2}(-)^m\cos(\frac{m\pi}{a}(x_1+x_2))$$

Let

$$\begin{cases}x_1-x_2=y_1\cdot\frac{a}{\pi}\\ x_1+x_2=y_2\cdot\frac{a}{\pi}+a\end{cases}$$

$$q'=q\cdot\frac{a}{\pi}$$

to obtain

$$P=\frac{1}{2}C\cdot\left(\frac{a}{\pi}\right)^2\cdot\sum_{m=1}^{\infty}\frac{1}{q'^2+m^2}\cos(my_1)-\frac{1}{2}C\cdot\left(\frac{a}{\pi}\right)^2\cdot\sum_{m=1}^{\infty}\frac{1}{q'^2+m^2}\cos(my_2)$$

$$=\frac{1}{2}C\cdot\left(\frac{a}{\pi}\right)^2\cdot\left(B(y_1,q')-B(y_2,q')\right)$$

where

$$B(x,q)=\sum_{m=1}^{\infty}\frac{\cos(mx)}{q^2+m^2}.$$

Now we calculate B(x,q):

$$B(x,q)=\sum_{m=1}^{\infty}\frac{\cos(mx)}{q^2+m^2}$$

$$=\operatorname{Re}(\sum_{m=1}^{\infty}\frac{e^{imx}}{m^2+q^2})$$

$$=\operatorname{Re}(\sum_{m=1}^{\infty}\frac{e^{imx}}{2iq}(\frac{1}{m-iq}-\frac{1}{m+iq}))$$

$$=\operatorname{Re}(\sum_{m=1}^{\infty}\frac{1}{2iq}\cdot\frac{1}{m-iq}\cdot e^{imx})-\operatorname{Re}(\sum_{m=1}^{\infty}\frac{1}{2iq}\cdot\frac{1}{m+iq}\cdot e^{imx})$$

$$=\operatorname{Re}(\sum_{m=1}^{\infty}\frac{1}{2q}\cdot\frac{1}{i(m-iq)}\cdot e^{i(m-iq)x}\cdot e^{-qx})-\operatorname{Re}(\sum_{m=1}^{\infty}\frac{1}{2q}\cdot\frac{1}{i(m+iq)}\cdot e^{i(m+iq)x}\cdot e^{qx})$$

$$=\operatorname{Re}(\frac{e^{-qx}}{2q}\cdot\sum_{m=1}^{\infty}\frac{1}{i(m-iq)}\cdot e^{i(m-iq)x})-\operatorname{Re}(\frac{e^{qx}}{2q}\cdot\sum_{m=1}^{\infty}\frac{1}{i(m+iq)}\cdot e^{i(m+iq)x})$$

Let

$$f(x,q)=\sum_{m=1}^{\infty}\frac{1}{i(m-iq)}\cdot e^{i(m-iq)x}$$

$$f(x,-q)=\sum_{m=1}^{\infty}\frac{1}{i(m+iq)}\cdot e^{i(m+iq)x}$$

Then

$$\frac{\partial}{\partial x} f(x,q) = \sum_{m=1}^{\infty} e^{i(m-iq)x} = e^{qx} \sum_{m=1}^{\infty} e^{imx}$$

$$= e^{qx} (\frac{1}{2} \sum_{n=-\infty}^{\infty} \delta(\frac{x}{2\pi} + n) - F(q))$$

Where $F(q)$ is a function independent of x, to be determined later.

$$\mathrm{Re}(f(x,q)) = \int^{x} \sum_{n=-\infty}^{\infty} \frac{1}{2}\delta(\frac{x}{2\pi} + n) - F(q)) \cdot e^{qx} dx$$

$$= \sum_{n=-\infty}^{\infty} \int^{x} \pi\delta(x + 2n\pi) e^{qx} dx - \int^{x} e^{qx} F(q) dx$$

$$= \sum_{n=-\infty}^{\infty} \pi\Theta(x + 2n\pi) e^{-q\cdot 2n\pi} - \frac{F(q)}{q} \cdot e^{qx}$$

$$= \pi \sum_{n=C(\frac{-x}{2\pi})}^{\infty} e^{-2n\pi q} - \frac{F(q)}{q} \cdot e^{qx}$$

$$= \pi \cdot \frac{e^{-2\pi C(\frac{-x}{2\pi})}}{1 - e^{-2\pi q}} - \frac{F(q)}{q} \cdot e^{qx}$$

Where $C(x)$ is the ceiling function returning the minimum integer larger than x.

Let $x = 0$, then:

$$f(0) = \sum_{m=1}^{\infty} \frac{1}{i(m - iq)}$$

So

$$\frac{F(q)}{q} = \mathrm{Re}\left(\sum_{m=1}^{\infty} \frac{1}{i(m - iq)} \right) - \frac{\pi}{1 - e\,-^{2\pi q}}$$

Thus

$$\mathrm{Re}(f(x,q)) = \pi \frac{e^{-2\pi C(\frac{-x}{2\pi})} - e^{xq}}{1 - e^{-2\pi q}} + \sum_{m=1}^{\infty} \frac{q}{m^2 + q^2} \cdot e^{qx}$$

Then

$$B(x,q)=\frac{e^{-qx}}{2q}\mathrm{Re}(f(x,q))-\frac{e^{qx}}{2q}\mathrm{Re}(f(x,-q))$$

$$=\frac{1}{2q}\left\{\pi\,\frac{e^{(-2\pi C(\frac{-x}{2\pi})-x)q}-1}{1-e^{-2\pi q}}+\frac{\operatorname{csc}h(\pi q)\left[\pi q\cosh(\pi q)-\sinh(\pi q)\right]}{2q}\right.$$

$$\left.-\pi\,\frac{e^{(2\pi C(\frac{-x}{2\pi})+x)q}-1}{1-e^{2\pi q}}+\frac{\operatorname{csc}h(-\pi q)\left[-\pi q\cosh(-\pi q)-\sinh(-\pi q)\right]}{2q}\right\}$$

Then

$$P=\frac{1}{2}C\cdot\left(\frac{a}{\pi}\right)^2\cdot\left(B(y_1,q')-B(y_2,q')\right)$$

$$=\frac{1}{2}C\cdot\left(\frac{a}{\pi}\right)^2\cdot\frac{1}{2q'}\cdot$$

$$\left\{\frac{e^{-(2\pi C(\frac{-y_1}{2\pi})+y_1)q'}-e^{-(2\pi C(\frac{-y_2}{2\pi})+y_2)q'}+e^{-(2\pi C(\frac{-y_1}{2\pi})+y_1)q'-2\pi q'}-e^{-(2\pi C(\frac{-y_2}{2\pi})+y_2)q'-2\pi q'}}{1-e^{-2\pi q'}}\right\}$$

$$=\frac{aC}{4q}\cdot\left\{\frac{e^{(-2C(\frac{x_2-x_1}{2a})aq-(x_1-x_2)q)}-e^{(-2C(\frac{a-x_1-x_2}{2a})aq-(x_1+x_2-a)q)}}{1-e^{-2aq}}\right.$$

$$\left.+\frac{e^{(2C(\frac{x_2-x_1}{2a})aq+(x_1-x_2)q-2aq)}-e^{(2C(\frac{a-x_1-x_2}{2a})aq+(x_1+x_2-a)q-2aq)}}{1-e^{-2aq}}\right\}$$

Let $x_2 > x_1$, due to the symmetry

$$P=\frac{\hbar}{\varepsilon_0}\cdot\frac{\partial\omega}{\partial\varepsilon_i(w)}\cdot\frac{1}{2q(1-e^{-2aq})}$$

$$\left\{\exp^{(x_2-x_1-2a)q}-\exp^{(-x_2-x_1-a)q}+\exp^{(-x_2+x_1)q}-\exp^{(x_2+x_1-a)q}\right\}$$

Or more generally, in an arbitrary region which

$$x_1, x_2 \in (a, b)$$

And let

$$\Sigma \equiv x_1 + x_2$$

$$\Delta \equiv \left| x_1 - x_2 \right|$$

And L^2 be the cross section of the structure.

Then

$$P = \frac{\hbar}{L^2 \varepsilon_0} \cdot \frac{\partial \omega}{\partial \varepsilon_i(w)} \cdot \frac{1}{2q(1 - e^{-2(b-a)q})}$$

$$\left\{ e^{(\Delta - 2(b-a))q} - e^{(-\Sigma + 2a)q} + e^{(-\Delta)q} - e^{(\Sigma - 2b)q} \right\}$$

Given correlation function, we also can generate coupling potential in real space

$$M(x) = \frac{e^{-aq} - e^{-2xq}}{e^{-aq} - e^{-(2x-2b)q}} e^{qb} M(x-b) + \eta \sqrt{\frac{(e^{-aq} - e^{-2xq})(e^{2bq} - 1)}{q(e^{-aq} - e^{-(2x-2b)q})}}$$

that has on average the same correlation as real potential, where η is a random number such that $\left\langle \eta^2 \right\rangle = 1$.

For the interface modes, we use the sampled coupling potentials of the interface modes directly to generate the correlation functions.

3.3.3 Device Model

Intersubband injection lasers operate on the condition that phonon-assisted interwell electronic transitions provide a fast depopulation of the final states of the optical transition allowing population inversion [35]. Although both cascaded and non-cascaded designs have been successfully implemented, the essential element, two quantum wells separated by a tunnel barrier, is the same, as illustrated in Figure. 3.9. To optimize the carrier transport through the barrier, the quantum wells are designed such that the lower subband of leading quantum well (the narrower of the two quantum wells in the exampled of Figure 3.9) and the first excited subband of the trailing quantum well (the wider well in the example of Figure 3.9) are nominally degenerate allowing for coherent quantum mechanical tunneling between wells. To optimize phonon scattering the energy separation between the ground and excited state of the trailing well are tuned according to the phonon energies [36-43]. Previously, Golden Rule (GR) based calculations have been used to carefully examine the effects of variations in the well widths and of the various types of phonon modes involved, interface and confined, on this process [13]. In this work, non-equilibrium Green's function (NEFG) based calculations with scattering are used to extend this study by examining the essential effects of variation of the barrier thickness.

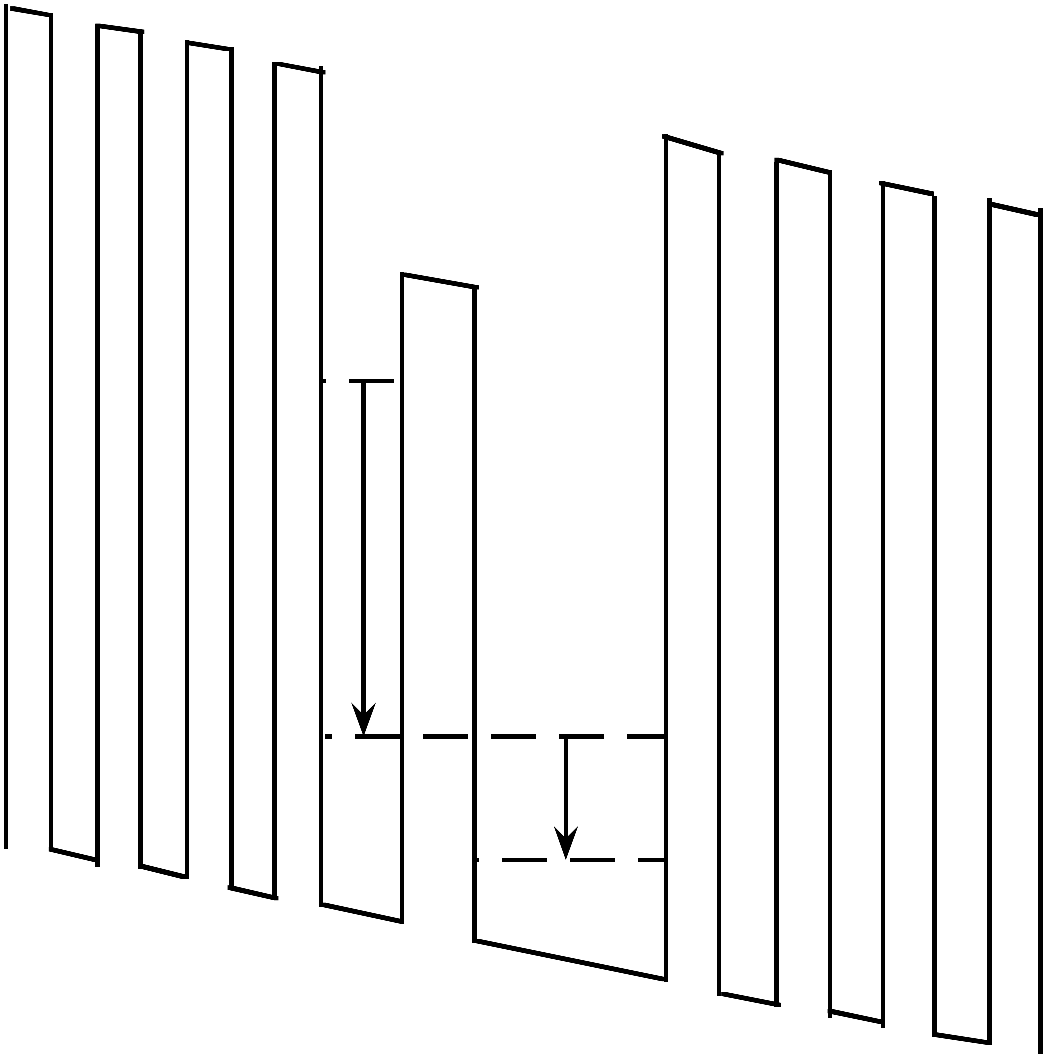

Figure 3.9: A typical quantum-well laser structure. The left arrow shows the optical emission and the right arrow shows the phonon emission.

The indicated switch from a GR-based analysis to a true quantum transport calculation is inherently necessary to achieve the above goal over the full range of barrier thicknesses considered (although the use of simpler models may be possible in various limiting cases), and demonstrating and explaining this need is a secondary goal of this work. Under the ideal resonance condition, the energy eigenstates associated with the ground subband of the first well and the first excited subband of the second well are, in fact, delocalized among the two wells, a result that is independent of the barrier thickness even if harder to achieve for thicker barriers. Under these conditions the GR calculation neglects the time required for coherent tunneling between the wells via the implicit application of the random phase approximation (RPA) among the intermediate states, as is elaborated on in the “Results” section to follow. This is a reasonable approximation for sufficiently thin barriers. However, as the barrier becomes thicker, the inter-well tunneling time will become a significant and then the dominant limitation on depopulation of the final state of the optical transition.

To isolate the essential physics we have used the basic square-well potential structure, if not precise numerical values, that was used previously in the GR-based analysis of this system, Ref. [13], as shown in Fig. 3.10 for one particular set of well and barrier widths. We have also used an envelope function approximation for the electrons and the macroscopic model of the phonon modes employed in Ref. [13]. The electron effective masses and non-parabolicity constants for the well and barrier materials, and the parameters used to calculate the confined, interface and half-space phonon modes and their interaction with electrons in SEMC are given in Table 3.2. Note that in actual intersubband lasers, whatever the actual well widths discretized in terms of atomic layers, resonance between the wells is achieved through adjustment of the potential drop across the device, as illustrated in Fig. 3.9. In the square-well model system of Ref. [13], for modeling purposes it was achieved through adjusting the well widths continuously. Here, subject to the constraints of a discrete lattice required for the SEMC calculations, once the system was near resonance, the dept of the first well was adjusted to fine tune the resonance when required to retain (by choice not necessity) the square-well nature of the model.

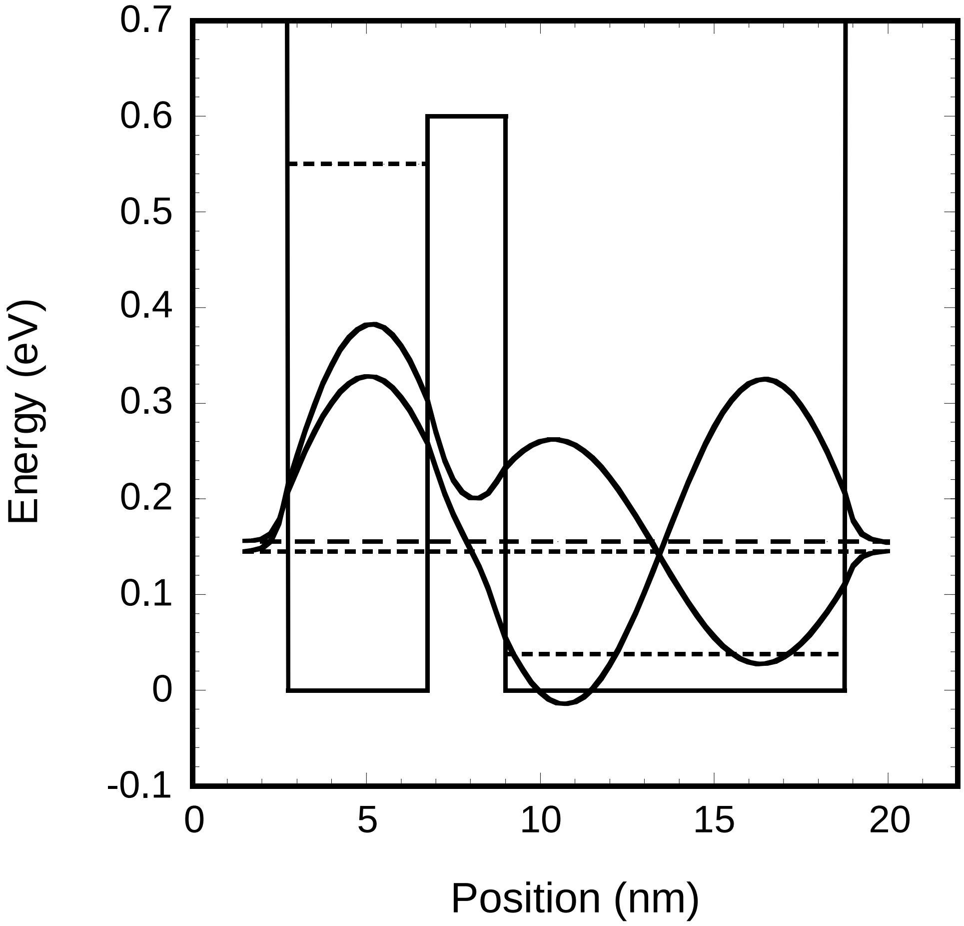

Figure 3.10: Band diagram and energy levels of an AlAs/GaAs double quantum well heterostructure. Here, the ground state of the first well is aligned with the first excited state of the second (in the limit of large barrier thicknesses) to maximize inter-well tunneling. The two delocalized energy eigen-functions resulting from this alignment are also shown (with the zero reference for the each eigen-function aligned to its respective energy eigenvalue).

	*M**	Nonparabolicity	ε(high)	ε(low)	ω(LO)/meV	ω(TO)/meV
GaAs	0.067	0.61	12.90	10.89	36.25	33.29
AlAs	0.14	0.25	8.15	10.90	50.09	44.88

Table 3.2: Effective Mass, nonparabolicity constant, dielectric constant, and phonon frequencies used in this work [44].

We injected carriers, actually a carrier probability current, into the simulation region via photon emission using the usual electron photon interaction Hamiltonian $H \propto (n_{photon} + 1)\hat{\mathbf{A}} \cdot \hat{\mathbf{p}}$ operating on the well-localized excited state wave-function of the first well to define the source term $\mathrm{A}(\mathbf{r}, E)$, where $\hat{\mathbf{A}}$ is a unit vector in the direction of the vector potential which is assumed to be normal to plane of the well here, $\hat{\mathbf{p}}$ is the momentum operator operating on the electron coordinate, and n_{photon} is the photon occupation number representing the, here arbitrary, intensity of the light. The energy E in the above equations and here is the excited state energy of the first well minus the photon energy $\hbar\omega_{\mathrm{photon}}$. To isolate the essential physics I have taken the 0 K temperature limit so that the only way out of the first well in these simulations is, roughly speaking, via tunneling through the barrier and down to the ground subband of the second well via phonon emission where the probability current is then absorbed via a complex potentials $\Omega(\mathbf{r}, n_1, ..., n_q - 1, ..., n_Q)$ representing subsequent scattering as described in Chapter 2.

Of course other scattering mechanisms, such as acoustic phonon scattering, carrier-carrier scattering, interface roughness scattering, impurity scattering etc. could aid in the depopulation of the final state of the optical transition. However, the essential limitation of the GR-based calculations for these processes would be the same. On the other hand, when the wells are not in resonance and the intermediated states become much more localized to one well or the other, the artifacts of GR calculations considered in this work would be at least reduced. However, under this latter condition, the depopulation rate would be less than optimal and the interwell transitions themselves would likely mediated by the various scattering processes (which is actually included in the calculations here for optical phonon emission). Our goal in this work is to isolate and address the essential physics of the optimal processes intended by design.

3.3.4 Simulation Results

The energy states within two wells as a function of the first well width **a** are shown in Fig. 3.11, for the specific case of a 2 nm barrier and the second well of 10 nm width. The resonance between the ground state in the first well and the first excited state in the second well occurs at a = 4.25 nm where the anticrossing is found. Or at least it does so to within the spatial resolution of the code; again a small adjustment to the potential in the first well was made to optimize the resonance at this point.

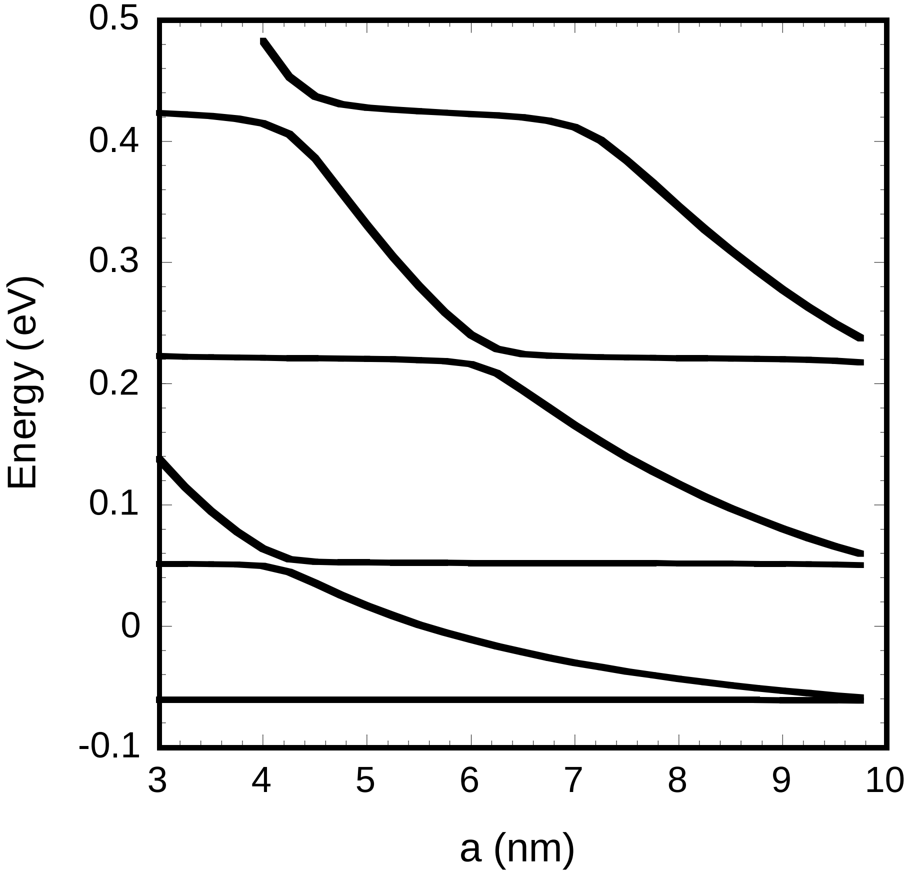

Figure 3.11: Subbands in the double-well structure as a function of **a**, the first well width, for fixed barrier width (2 nm) and second well width (10 nm). Except near the anti-crossings, the width-dependent energies are of course those of states localized predominately to the first well, and the width independent energies those of state localized predominately to the second well.

The transition rates from the intermediate state after photon emission in the first well to the final, ground state localized to the second well—calculated as the probability current flow out of the intermediate state divided by the probability density in the intermediated state—are shown in Fig. 3.12 as a function of the width of the first well. For this figure and Fig. 3.13 the photon energy is chosen as that for which the injection current is greatest, which as expected is roughly the energy separation between what would be the well-defined ground and first-excited states of the first well in the absence of the tunneling and scattering that broaden these states in SEMC. In this calculation, both interface and confined phonon modes are considered as in Ref. [13]. Our results for the 2 nm barrier show a close coincidence (both in shape and peak of the curve) with the result obtained in the GR-based Calculations of Ref. [13]. As expected, the total transition process, photon emission followed by phonon emission, from the excited state localized to the first well to the ground state localized to the second well is optimized at this anticrossing where the intermediate states—the final state for the optical transition and the initial state for phonon scattering—are delocalized among the two wells. For GR calculations, however, this is simply because the intermediate state wave functions significantly overlap both the initial and final states. There is no direct consideration of the tunneling time. As a result, at the anticrossing, the GR calculations simply saturate for large well thicknesses as shown in Fig. 3.13.

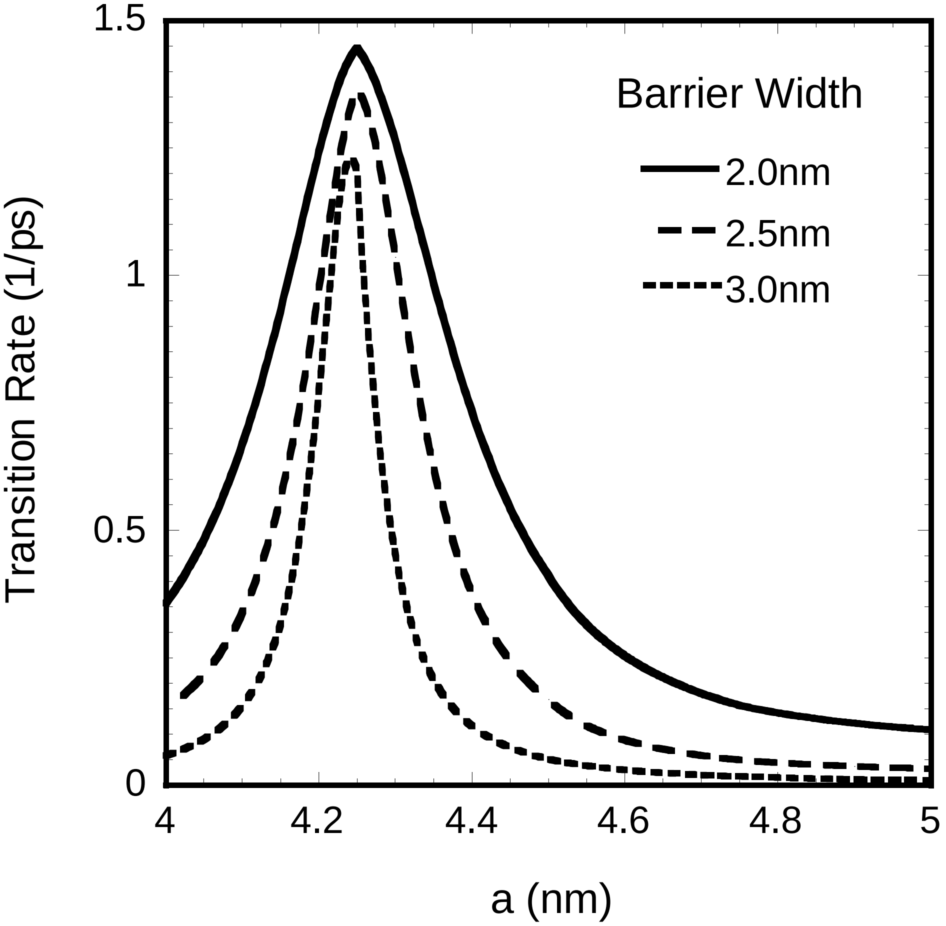

Figure 3.12: Interwell polar optical-phonon-assisted transition rate under the double electron-phonon resonance condition as a function of **a**, width of the first well, with the second well width fixed at 10 nm. As the barrier becomes thicker, not only does the resonance width decrease but the peak transition rate decreases as well.

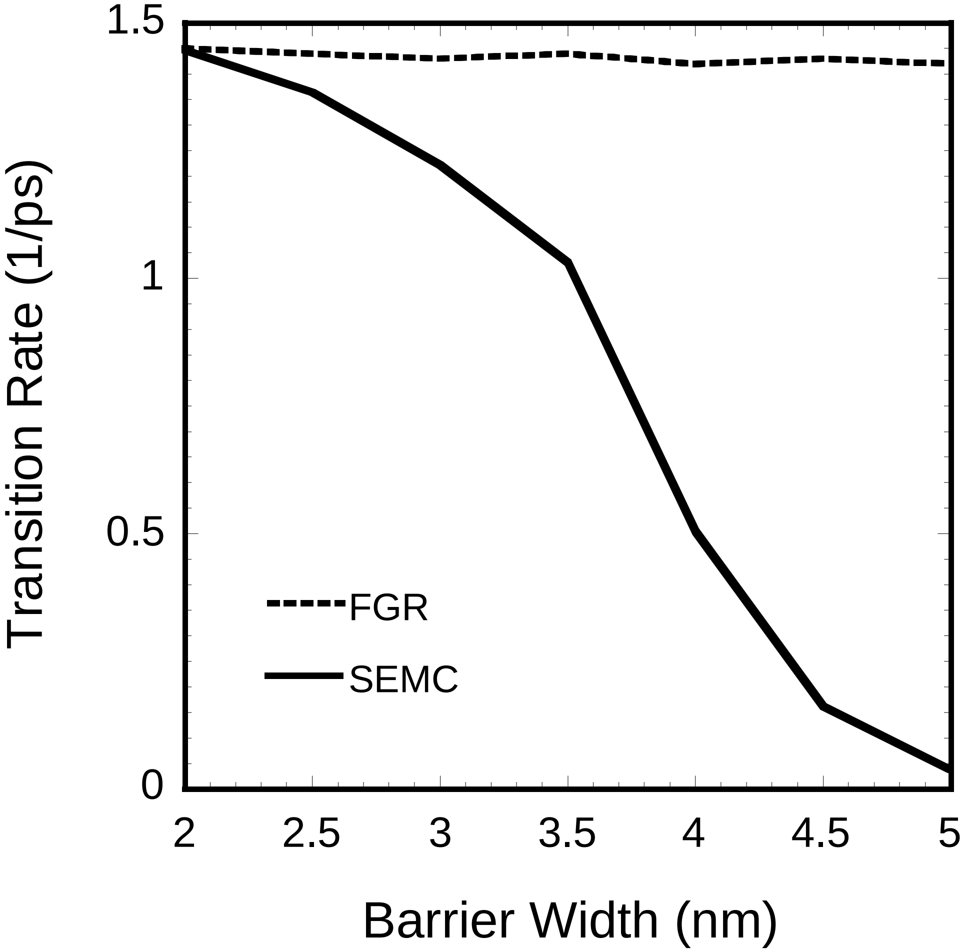

Figure 3.13: Maximum transition rate, occurring at the anticrossing, as a function of barrier width for SEMC and GR calculations. Note that the GR results are essentially unaffected by the barrier width while for SEMC calculations the transition rate falls as tunneling becomes the limiting process.

However, also as shown in Fig. 3.13, as the barrier width increases the corresponding transition rate decreases rapidly in the SEMC calculations. At a 2 nm barrier width, the GR and SEMC give nearly the same results, while by time the barrier thickness goes to 5 nm, the SEMC calculations give a transition rate of approximately 3% of that obtained via the GR approximation. The reason for the discrepancy is, again, that tunneling through the interwell barrier limits the depopulation rate of the intermediate state. Roughly speaking, for thick barriers at least, there are three processes to consider each of which takes time, as illustrated in Fig. 3.14(b) and shown in via the SEMC simulation of Fig. 3.15: Photon emission first takes the electron to one or the other or, particularly for thicker barriers, a coherent overlap of the two roughly degenerate states at the anti-crossing that is localized to the first well. The electron then propagates to the second well via tunneling (roughly in a time commensurate with the energy level splitting). Then finally, the electron now within the second well emits a phonon to be captured in the ground state that is localized to the second well. Of course in reality, and in SEMC, these individual processes are not so well separated. In contrast, the random-phase approximation among energy eigenstates implicit to the GR — GR calculations provide the squares of the magnitudes of the amplitude coefficients of the eigenstates only, ignoring any coherence between differing initial and/or differing final states — places carriers in an incoherent overlap of the intermediate states which, as a result, already overlaps the second well in position immediately after "completion" of the photon emission regardless of barrier thickness. As a result the three-step process of Fig. 3.14(b) is artificially turned into a two-step process, as illustrated in Fig. 3.14(a); the time to tunnel through the barrier is not considered regardless of the barrier thickness. The fallacy of this latter result is self-evident if one considers huge wells separations of, e.g., a micron, but it becomes important at only a few nanometers as shown by Fig. 3.13. This neglect of the time required for real-space transport is a common failure mode for the GR approximation when initial and final states are not localized to the same region as in [6] and section 3.2.

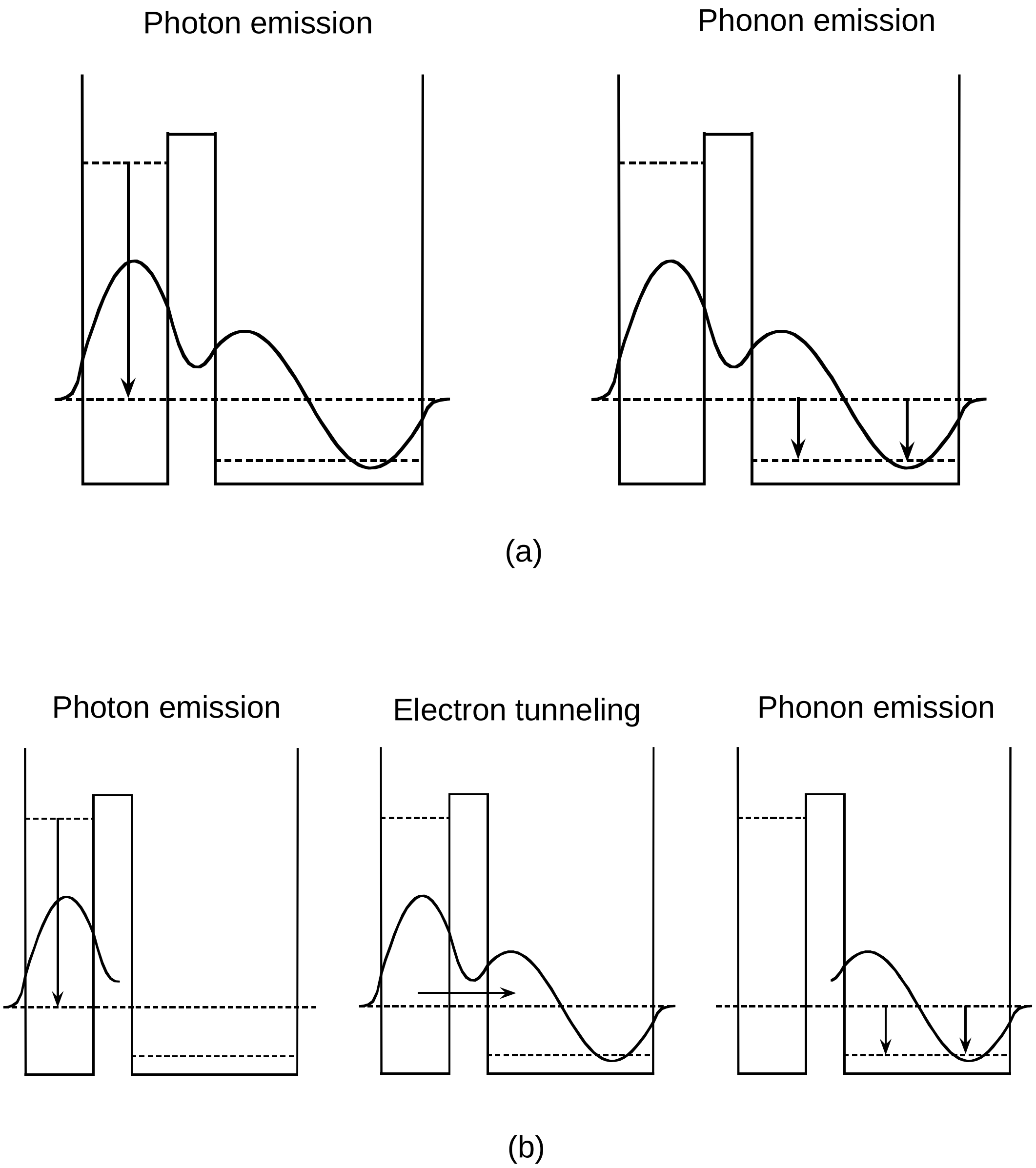

Figure 3.14: Illustration of physical processes considered via the GR assumption, and via SEMC. (a). In GR calculations only two physical processes are considered: photon emission to one of the two delocalized intermediate state is followed directly by the phonon emission from that the intermediate state to the final state localized in the second well. (b). SEMC addresses three physical processes: photon emission, real-space transport/tunneling through the barrier and phonon emission.

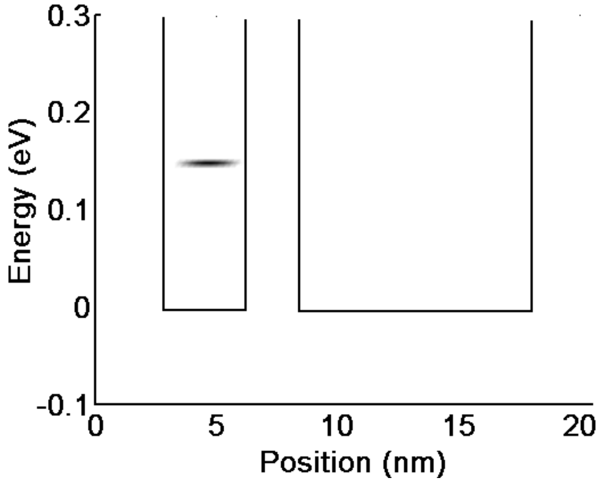
0.3
0.2
0.1
0
-0.1
Energy (eV)
0
5
10
15
20
Position (nm)

(a)

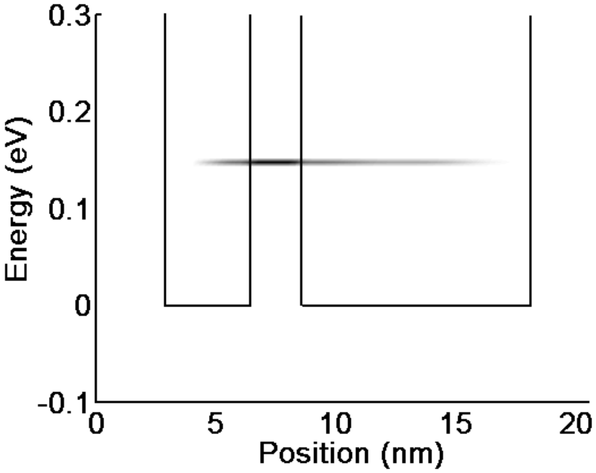
0.3
0.2
0.1
0
-0.1
Energy (eV)
0
5
10
15
20
Position (nm)

(b)

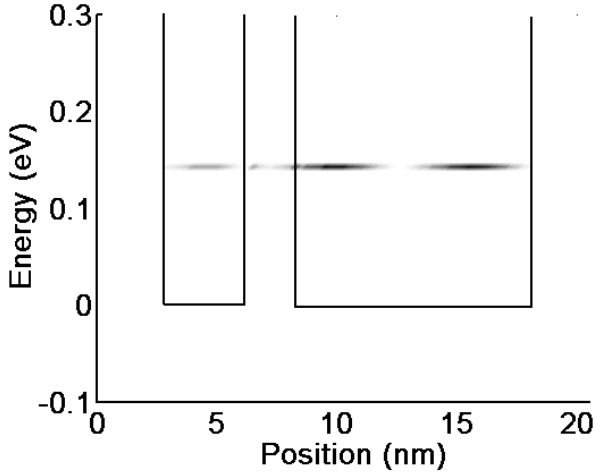
0.3
0.2
0.1
0
-0.1
Energy (eV)
0
5
10
15
20
Position (nm)

(c)

Figure 3.15: Current flow in the double-quantum-well laser given by SEMC simulation for fixed photon energy as a function of the intermediate state energy and position for a 2nm barrier, with darker areas indicating greater current flow: (a) probability flow into the intermediate state due to photon emission, (b) real-space probability current flow to the right after photon emission and before phonon emission, and (c) probability flow out of the intermediate state energy state due to phonon emission. Solid lines represent the well potential structure (at $k||$ = 0). The nonzero energy widths of these contours and the residual phonon emission within the first well seen in (c) result from the homogeneous broadening of the electron states.

In addition to affecting the transition rate between wells, the barrier thickness affects the photon emission rate as well, as shown in Fig. 3.16. As the thinner barrier leads to an increased depopulation rate for the intermediate states, it also inherently leads to an increase in homogeneous (energy/collision/finite-lifetime) broadening of the photon transition to the intermediate states. This homogeneous broadening, in turn reduces the peak photon emission rate per electron in the excited state of the first well, a peak that would be aligned to the lasing frequency, at least to within the width of the laser line and the non-homogeneous broadening in the system. The reduced photon emission rate combined with the increased phonon emission rate as the barrier narrows should actually further enhance population inversion. However, the reduction in photon emission rate could also reduce gain both by itself and, particularly near threshold, by increasing the relative importance of parasitic dark recombination mechanisms competing with photon emission that are not sensitive to the final state broadening, such as large angle phonon scattering, carrier-carrier scattering.

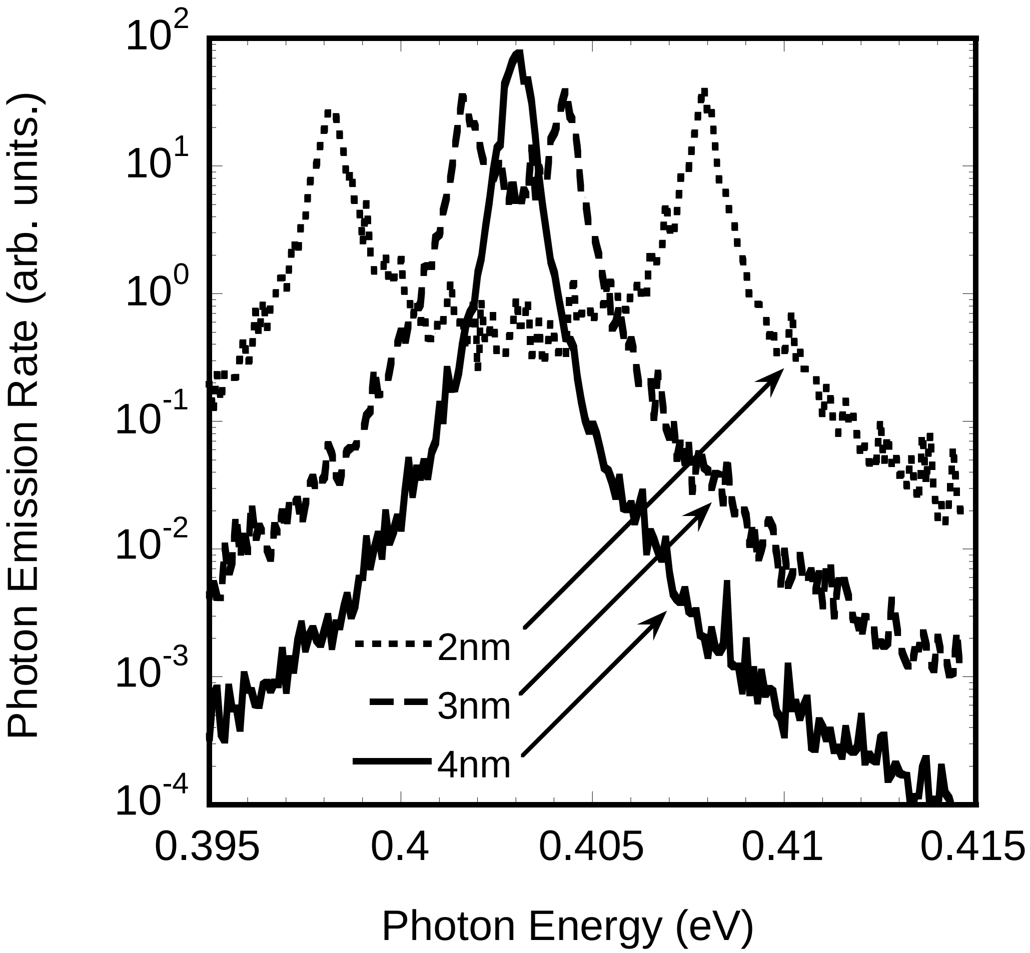

Figure 3.16: Rate of photon emission as a function of photon energy (arbitrary units) for different barrier widths. The noise in the figure is a result of the Monte Carlo technique used to model scattering. Note that when the barrier is thin and the wells strongly coupled and phonon emission limits the transition rate out of the intermediate states (2 and 3 nm well widths; See Fig. 3.13), two intermediate states of almost barrier-width-independent amplitude and width are well resolved. However, when the barrier becomes thicker and tunneling begins to limit the transition rate (4 nm well width), the two states overlap and the phonon emission peak becomes narrower and stronger at the peak with the decreasing broadening of the intermediate state.

3.3.5 Conclusion

Using the NEGF quantum transport code SEMC, it has been shown that the barrier thickness plays an important role in multi-well quantum lasers not evident via Fermi-Golden Rule calculations. In the simple illustrative case considered here, only one barrier and two wells, the GR-based calculations can produce large overestimates in the expected rate of depopulation of the final state for photon emission for relatively thick barriers. Accordingly, sufficiently thin barriers must be maintained to optimize population inversion. Furthermore, as the well thickness is decreased, the increase in homogeneous broadening of the intermediate states associated with their increased depopulation rates reduces the peak photon emission rate. This, in turn, actually further aids population inversion but could ultimately reduce gain in and of itself and by increasing the relative importance of parasitic dark recombination mechanisms. Therefore, in addition to choice of, in particular, the trailing well width as discussed in Ref. [13], the barrier width must be optimized for peak performance, and in a manner not readily apparent through GR-based calculations alone.

CHAPTER 4. QUANTUM TRANSPORT IN DOUBLE GATE MOSFETS: EFFECT OF QUANTUM NONLOCALITY ALONG THE CHANNEL ON TRANSCONDUCTANCE IN THE BALLISTIC LIMIT

4.1 INTRODUCTION

In the past decade, the dimensions of MOSFETs have been scaled deep into the sub-0.1μm regime [45-48]. Quantum mechanical effects are expected to become more and more important. Accurate quantum transport simulations will be needed to explore the essential device physics and as design aid. In this chapter, SEMC-2D, which provides an electrostatically self-consistent treatment of quantum transport with realistic scattering, was used to study the carrier transport in nano-scaled double gate MOSFETs. The purpose of this study was to explore the effects of quantum non-locality along the channel essential on carrier transport and scattering in such a nano-scaled MOSFET device.

In this work, we model transport in, specifically, ultra thin body double gate SOI structure [49, 50]. These have been proposed as a promising candidate to replace the conventional device structure as the device dimensions continue to scale down. This is because that two gate electrodes control the channel jointly and screen the drain field away from the channel more effectively than in conventional devices [51].

4.2 THE INJECTION EFFICIENCY THEORY

MOSFET drain current density per unit gate width can always be written as the product of n_{top}, the carrier sheet charge density at the top of the source-channel barrier, which is controlled by the gate in a truly well-tempered MOSFET, and the average velocity of those carriers $\langle v_{top} \rangle$,

$$I_D = qn_{top} \langle v_{top} \rangle \tag{4.1}$$

where q is the magnitude of the electron charge and we have considered the case of an nMOSFET for specificity. With "thermal velocity" v_{th} defined — for compactness of expression and consistency with prior work [52-54] — as simply the average carrier velocity along the channel direction at the barrier top obtained in the ballistic limit for injection from a (half-space) thermal distribution of carriers in the source, the current can be written as

$$I_D = qn_{top} v_{th} \gamma \tag{4.2}$$

where

$$\gamma = \langle v_{top} \rangle / v_{th} \tag{4.3}$$

is the "injection efficiency" [53]. In the ballistic limit where scattering processes such as phonon emission and absorption of phonons and interaction with the 'rough' semiconductor-dielectric surface are absent or at least neglected, γ is unity; back-reflection from the channel due to such scattering process then reduces γ below unity. Thus, $qn_{top}v_{th}$ would represent the maximum obtainable drive current density in the MOSFET, which is clearly an important design consideration for nano-scale MOSFETs even if not an entirely reachable limit. As we illustrate momentarily, in a semi-classical transport analysis v_{th} is essentially a constant with gate voltage if a Boltzmann distribution of injected carriers is assumed or increases somewhat above threshold with increasing gate voltage due to increasing degeneracy when a Fermi distribution is assumed, leaving the drive current to vary primarily with changes in the, in "well-tempered" MOSFETs, gate-controlled carrier density n_{top}.

However, we have found that when non-local quantum transport effects along the channel are accounted for, this simple picture of transport is somewhat more difficult to employ. The thermal velocity v_{th}, as effectively defined via equation (4.1) and (4.2) in the ballistic limit, can vary significantly with gate voltage relative to its value obtained via a semiclassical transport analysis. Under some circumstances, v_{th} obtained from the quantum transport analysis actually can exceed that obtained from a semiclassical transport analysis (even allowing for Fermi statistics). This variation in thermal velocity is accompanied by variations in the drive current, as one might expect. However, in the not perfectly well tempered devices we simulated for this work — producing perfectly well tempered nano-scale devices as judged by quantum or even classical transport calculations is, at best, nontrivial — the current variations lag the thermal velocity variations in degree in the electrostatically self-consistent system due to opposing variations in the nominally gate-controlled charge density, even with Fermi statistics and quantum confinement effects normal to the transport direction considered in both the "semiclassical" and quantum mechanical transport analyses. In what follows, we describe the simulation procedure, present simulation results, and provide physical explanations for the variations in thermal velocity and drain current from the semiclassical expectations. We emphasize that we are not addressing the well known quantum-transport-related subthreshold leakage currents (e.g. [55]) in this work. Indeed, we consider the above threshold effect of interest in this work only in devices for which the subthreshold leakage currents are essentially unaffected; large subthreshold leakage currents would, of course, make above threshold behavior a moot issue.

We note that, although this work addressed the ballistic transport limit, we do not mean to discount the importance of scattering in these devices. Indeed, this work arose from a more complex work to gauge the reliability of semi-classical treatments of scattering (again with quantum confinement) by comparison to more rigorous quantum mechanical treatments that address carrier non-locality along the channel, a work that is still in progress. However, a baseline knowledge of the quantum transport in the ballistic limit is essential for this latter purpose, and, as noted above, ballistic transport remains of interest in itself as limiting behavior

4.3 QUANTUM AND SEMI-CLASSICAL TRANSPORT MODELS

The basic model device used in this work is a dual-gate ultra-thin body MOSFET shown in Fig. 4.1. In order to trace the difference between quantum and semi-classical transport, we have performed both a semiclassical Boltzmann transport (equation based) analysis [56,59] and a non-equilibrium Green's function (NEGF) analysis [60, 61] in the direction of transport, with scattering terms set to zero in both cases to consider the ballistic limit. However, in each case transport is subdivided by the subbands formed by quantum confinement normal to the channel, using the subband minimum energy as a function of position along the channel as the potential energy function; only the treatment in the transport direction is varied. The energy valleys are modeled as parabolic in both cases. Figure 4.2 shows the algorithm(s) including self-consistent solution of Poisson's equation for the potential profile for quantum and/or classical transport.

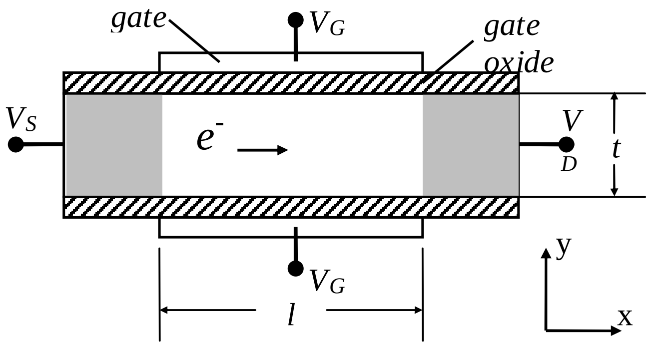

Figure 4.1: Model DGMOSFET with device parameters: channel length l = 10 nm, body thickness t = 3.0 nm, oxide thickness = 1.0 nm, source and drain lengths = 8 nm, source and drain doping = 10^{20}/cm^3, and channel doping = 0. The drain voltage was set to 0.5 V for all simulations.

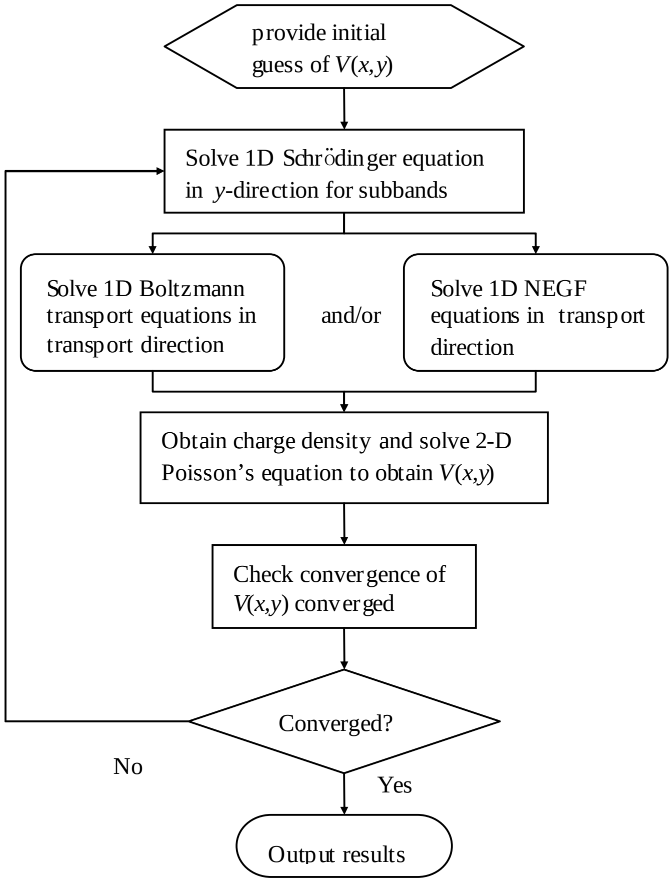

Figure 4.2: Simulation flowchart. Note that quantum confinement is considered for both quantum and "semiclassical" analyses.

4.4 RESULTS AND DISCUSSION

Fig. 4.3 shows the thermal velocities obtained from the quantum transport analysis and those obtained from the semi-classical analysis as a function of gate voltage for the 10 nm channel length, 3 nm body thickness device obtained assuming a Fermi distribution of injected carriers. Note that (as will be evident when we consider the current below, Fig. 4.6) the not too abrupt threshold occurs somewhere between gate voltages V_G of ±0.1 V, depending on how threshold is defined. In the simulations, we simply assumed the work function consistent with a p-type poly-silicon gate. (Developing gate materials with more appropriate work functions, is of course, another issue.) Shown for comparison in the inset of Fig. 4.3 over the same ranges are the results obtained using Boltzmann statistics for injected carriers. In the latter case, the very small variations in the thermal velocity in the semiclassical case result from slight relative variations in the occupancies of differently oriented energy valleys. The not insignificant increase in the semi-classical thermal velocity with gate overdrive seen for Fermi statistics that was mentioned earlier results from an increase in the Fermi level relative to the barrier top and the associated increase in the average energy of the thermal carriers. The variations seen in the quantum transport simulations which are still quite a bit larger cannot be explained in this way, however.

Before considering these differences between the semi-classical and quantum transport results for the thermal velocity, we begin by reprising and elaborating on the definition of thermal velocity. As stated in the first paragraph of the introduction, to remain consistent with Eqs (4.1) and (4.2), "thermal velocity" v_{th} is defined as the average carrier velocity along the channel direction at the barrier top obtained in the ballistic limit for injection from a (half-space) thermal distribution of carriers in the source for both the semiclassical and quantum transport calculations (where it is noted that the position of the barrier top can vary with transport model in these electrostatically self-consistent simulations). Furthermore, we point out that the definition of "velocity" used here is simply charge current divided by charge density for all calculations, quantum and semiclassical, as it must be to be consistent with Eq. (4.1). With this definition, the velocity of quantum mechanical particles of any energy at any position is well-defined even for carriers within the barrier. Notably, even in what is considered the ballistic limit — again, no phonon, surface roughness, etc. scattering — there is still some degree of reflection for carriers incident not only below but also above the barrier top in quantum transport simulations. In a sense, the wave-functions of the quantum mechanical carriers even as they pass the position of the barrier top contains both forward and backward traveling components where the latter can be thought of as providing a negative contribution to the velocity, although in practice these contributions cannot always be easily separated out of the wave-function particularly for carriers within the barrier — nor is there actually any need to do so here. In contrast, in the semiclassical transport limit, any carrier that actually reaches the position of the barrier top will have a unity transmission probability in the ballistic limit so that there is no contribution from a backward traveling component of negative velocity. In this work there has been no effort to compensate for this velocity "penalty" in the quantum transport analysis as such reflection is simply part of considering the ballistic limit. On the other hand, despite consideration of this reflected component in the quantum transport analysis, it is possible for the carrier velocity obtained from the quantum transport analysis to exceed that obtained from the semiclassical analysis. Anytime the transmission probability is nonzero and probability current flows, the carrier velocity will also be nonzero in the quantum transport analysis as the probability density must also remain finite. In particular, as a carrier with energy approaching that of the barrier top from above passes over the barrier top, although the velocity approaches zero as the probability density approaches infinity in the semiclassical analysis, the carrier's velocity remains quite large in the quantum transport analysis, as evident in the top portion of Fig. 4.4. Furthermore, the velocity obtained from the quantum transport analysis, a continuous function of the carrier energy, continues to exceed that obtained from the semiclassical analysis for a significant energy range above the barrier top, and remains nonzero within the barrier for tunneling carriers where, of course, velocity is undefined and irrelevant in the semiclassical analysis. Despite these conceptual complications, the definition of “thermal velocity” used in this work has been chosen to be consistent with Eq. (4.2) with the injection efficiency set to unity in the ballistic limit.

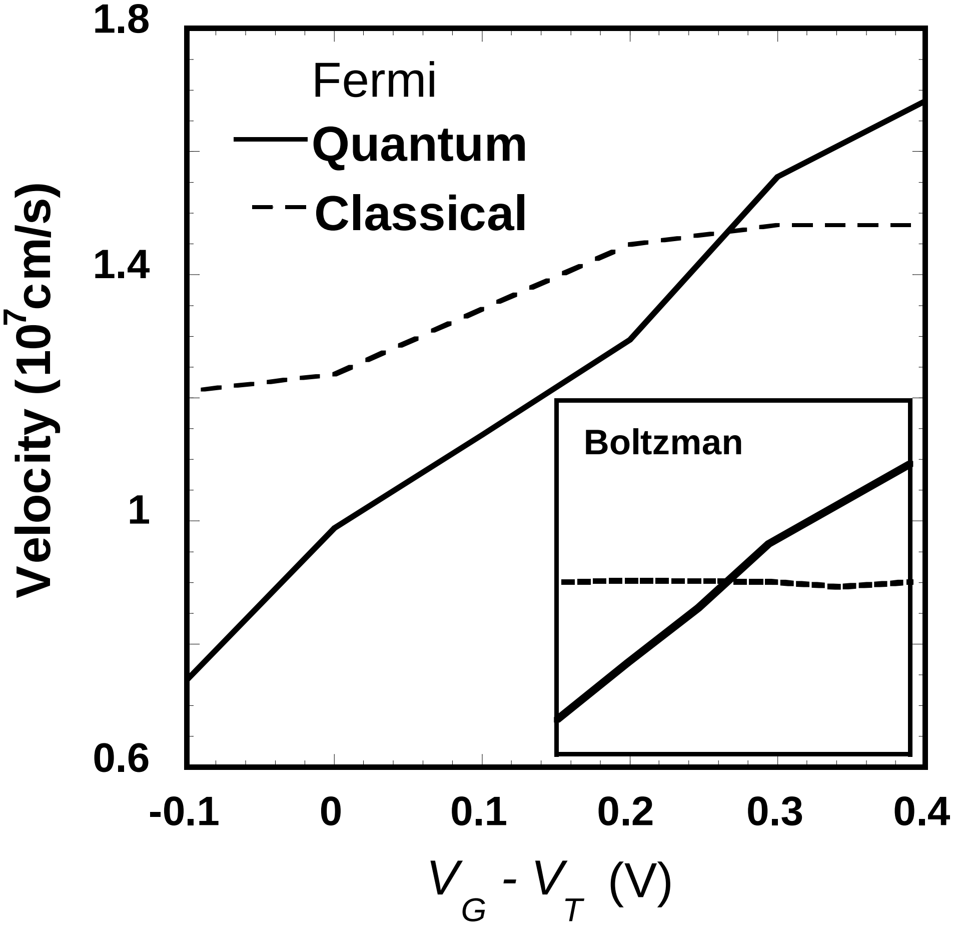

Figure 4.3: Average velocity of carriers at top of the barrier as a function of the gate overdrive V_G for semiclassical and quantum analyses obtained using a Fermi distribution of injected electrons from the source. The inset shows the even more pronounced results using a Boltzmann distribution of injected electrons for reference, with the same symbols and over the same voltage and velocity ranges.

To understand the difference between the semi-classical and quantum mechanical behaviors of thermal velocities we begin with the velocity of the electrons within the quantum mechanical treatment as a function of the carrier kinetic energy associated with motion along the channel at the spatial position of the barrier top, as shown in top portion of Fig. 4.4 for the above threshold gate voltages of V_G = 0.1 V and 0.4 V, with the classical energy dependence of velocity shown for reference. It can be seen that the velocity of the non-localized quantum mechanical electron not only does not go to zero at the barrier top energy as discussed above, but it is comparable to the classical thermal (average) velocity at that point, approximately 1.2×10^7 cm/s for V_G = 0.1 V gate and 1.5×10^7 cm/s for V_G = 0.4 V. The energy-dependent quantum mechanically calculated velocity also increases with the increase in gate voltage near and below the barrier top. The increase is a result of “sharpening” of the barrier that can be seen in the inset of Fig. 4.4, and which is of no consequence classically of course. Furthermore, as also shown in bottom portion of Fig. 4.4, the relative contribution from the low energy, low velocity tail of the tunneling current distribution is reduced as the increasing gate voltage decreases the barrier height. Again, there is no classical analog of this effect. Together, these two effects lead to the greater dependence of the thermal velocity on gate voltage in the quantum transport analysis seen in Fig. 4.3.

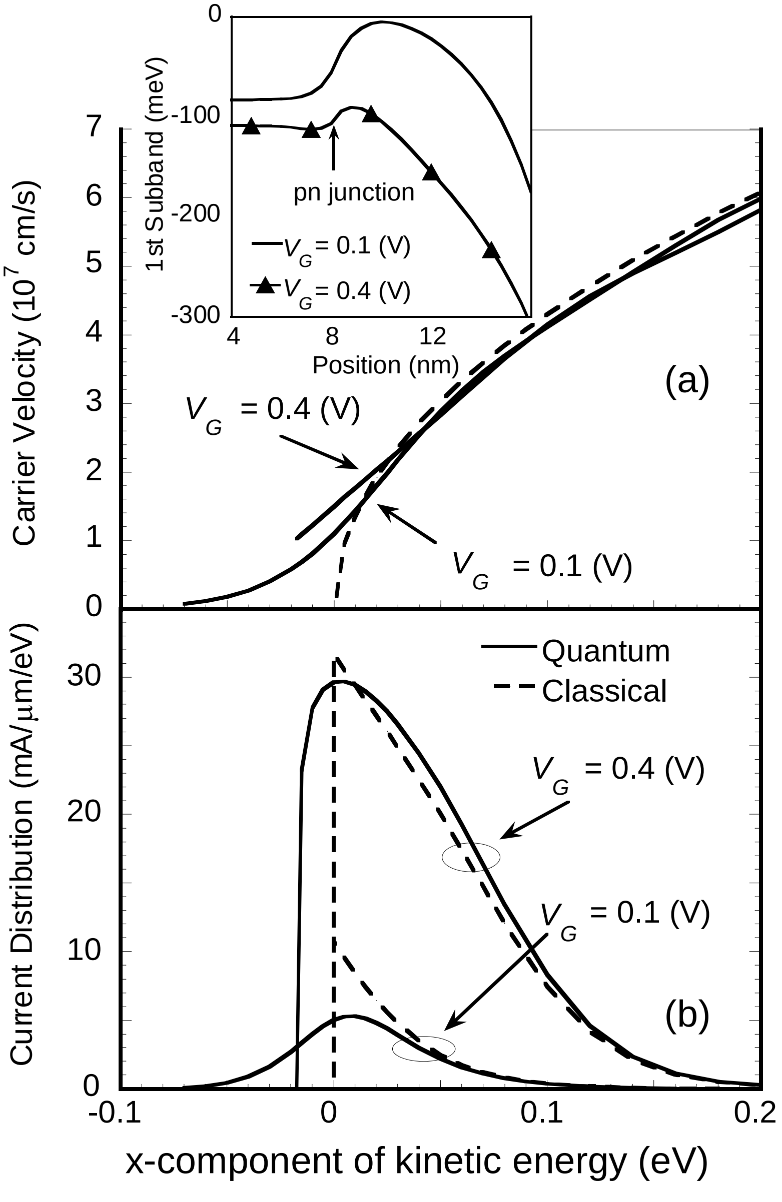

Figure 4.4: Electron velocity and current distribution as a function of the kinetic energy in the channel associated with motion in the transport (*x*) direction at the source-to-channel barrier top for the semiclassical and quantum analyses. For the quantum transport simulations, negative values of kinetic energy correspond to tunneling carriers, with the lowest values shown corresponding to the position of the ground state subband minimum in the source. The inset gives the ground-state subband energy profile along the

channel near the source-to-channel barrier top, where here the zero energy reference is the Fermi level. (The ground state subband energy is lower toward the source end at higher gate voltage due to reduced reflection and thus a lower subband position relative to the source-side Fermi level (voltage) to maintain charge neutrality in the leads.) The area under the curve of the energy dependent current of this figure provides the total current at the barrier top. As a control, for this figure and only for this figure (e.g., not for Fig. 4.3), the reference "semiclassical" current distributions were also obtained for the quantum mechanical potential profiles.

However, in these simulations, the increasing thermal velocity is partially offset by an opposite trend in the carrier density, as shown in Fig. 4.5 which provides ratios of the semi-classically calculated values to (what should be, in principle, the reference) quantum mechanically calculated values of thermal velocity, charge density and total current. These devices are clearly not perfectly well tempered, and it is as though the gate were struggling to maintain the charge density constant as the quantum mechanical carrier velocity increases or decreases relative to the classical value, and achieving only partial success. As noted above, producing perfectly well tempered nano-scale devices as judged by quantum or even classical transport calculations is problematic, particularly with significant quantum mechanical non-locality effects along the channel already evident in the former case. In addition, while the top of the barrier marks a clear disembarkation point in the classical case such that all of the carriers injected from the source that make it that far will be transmitted to the drain in the ballistic limit considered here, the barrier top position in the quantum mechanical case does not represent such a well defined disembarkation point due to quantum non-locality. For both of these reasons, while it is always possible to write the current in the form of Eq. (4.1), it appears to be an inconvenient consequence of scaling to nano-dimensions that prediction of drive current, ballistic or perhaps otherwise, via separate predictions of velocity and of charge density at the barrier top will become less quantitatively reliable (where it is noted that the analysis in Ref. [53] is explicitly described as semi-classical).

Nevertheless, as shown in Figs. 4.5 and 4.6 and consistent with qualitative expectations based on Fig. 4.3, the quantum mechanically calculated drain current is smaller than the semiclassically calculated value below a gate voltage of approximately 0.28 V and larger above. (Note that we were unable to converge the electrostatically self-consistent classical *ballistic* transport calculations — this is not the case with scattering considered — beyond a 0.45 V gate overdrive. Of course, for 10 nm devices the overdrive voltage shouldn't be much if any higher [62].) Also from Fig. 4.6, note that, as promised, the subthreshold slope obtained from the quantum transport analysis is essentially the same as that obtained from the semiclassical transport analysis.

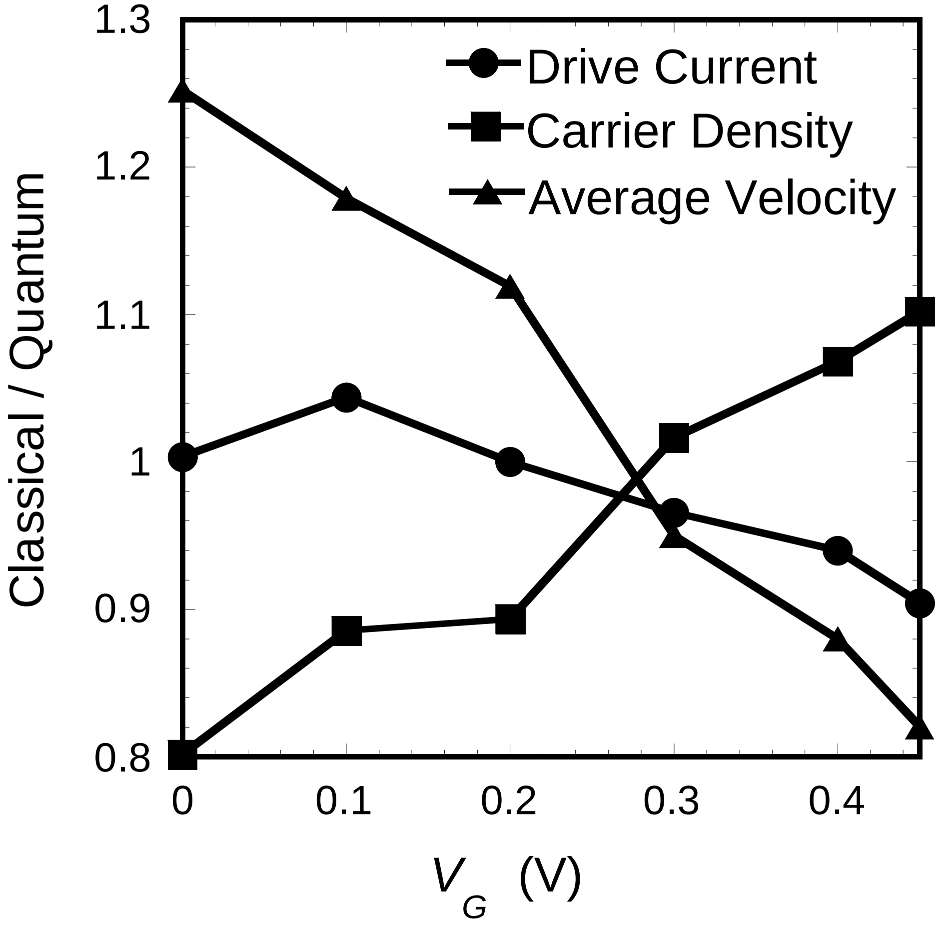

Figure 4.5: Ratios of semiclassically to quantum mechanically calculated thermal velocity (with absolute values shown in Fig. 4.3), charge density and total current for the 10 nm channel length device.

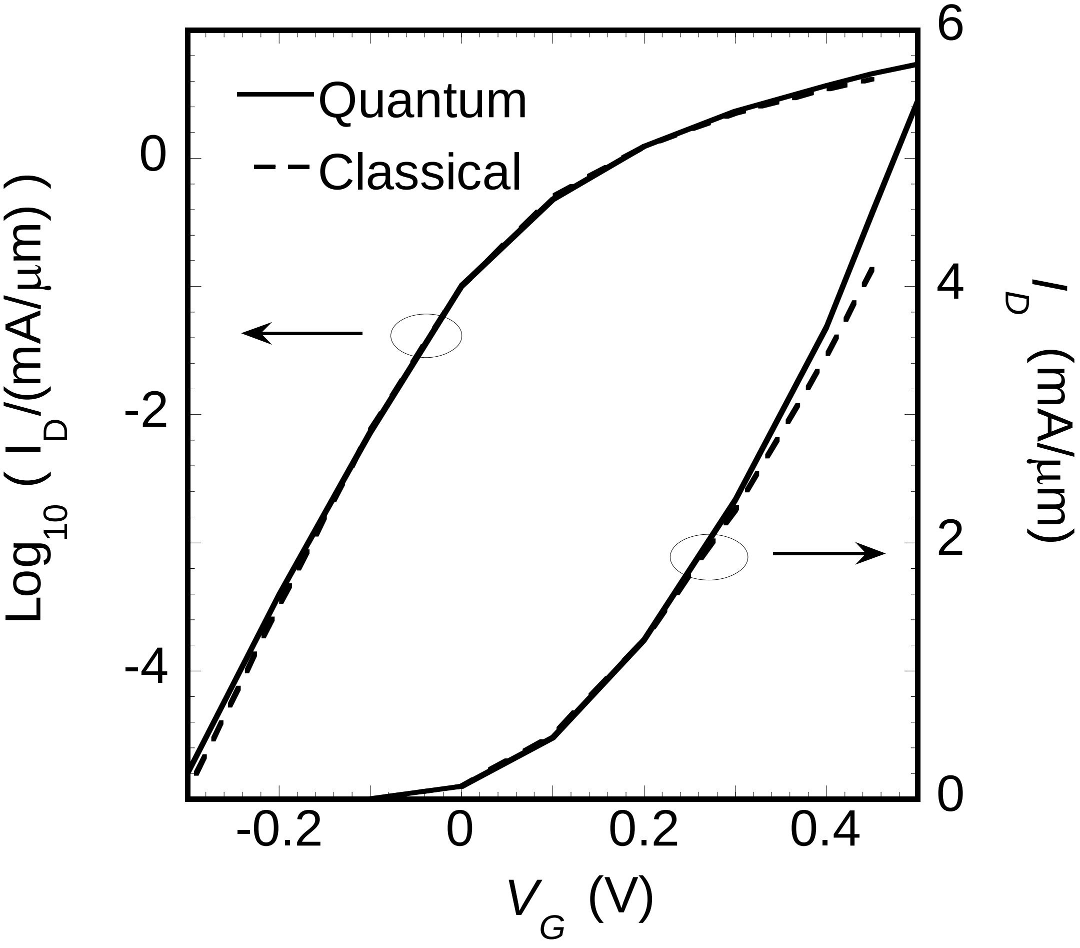

Figure 4.6: Quantum and semiclassical drive currents above and below threshold (which occurs somewhere approximately between $V_G = \pm 0.1$ V depending on how it is defined.) for the 10 nm channel length device.

The ratio of the semi-classically calculated drive current to the quantum mechanically calculated drive current was then considered as a function of the device size; Channel length *l*, body thickness *t* and oxide thickness were scaled in proportion up and down from that of the 10 nm channel length device considered above. (We have also considered more realistic graded doping profiles from MIT well-tempered devices [http://www-mtl.mit.edu/researchgroups/Well/] with and without gate overlap but qualitative results were much the same.) In the first set of simulations, the drain voltage, however, was held constant at 0.5 V to provide allow the semiclassical and quantum analyses to converge for larger devices as the source-to-channel barrier becomes thicker. Results, including from the device above, are shown in Fig. 4.7. Again, for each of these devices the subthreshold behavior was largely independent of the calculation method; only for a still smaller device is the subthreshold leakage behavior strongly affected by tunneling through the source-to-channel barrier, as shown in Fig. 4.8. However, in practice, larger devices will have larger drain voltages so we re-performed these calculations increasing the drain voltages with device size as shown in Fig. 4.9. Results suggest that quantum transport effects on ballistic transport could be significant for larger devices as well, were higher drain voltages can lead to barrier shapes comparable to smaller devices under lower drain voltages. Note that for Figs. 4.7 through 4.9, and for each device and method of calculation, we have somewhat arbitrarily defined the gate threshold voltage V_T as the voltage at which the drive current reaches 0.1 mA/μm. (For the 10 nm device by either quantum or classical analysis, V_T was essentially 0.0V; but V_T varied somewhat with device size and analysis method for the other devices.) Thus, the current ratios in these figures are unity at threshold simply by definition. It is interesting that quantum transport effects can actually improve transconductance above threshold, which may or may not provide an opportunity for design optimization not apparent through semi-classical transport analysis.

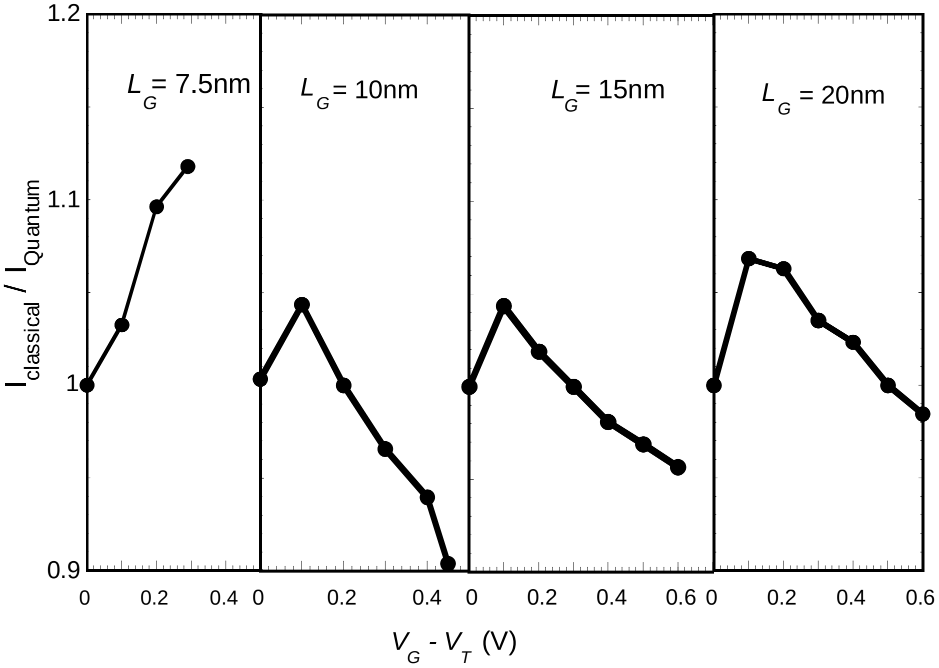

Figure 4.7: Ratios of semiclassically to quantum mechanically calculated current as a function of gate overdrive voltage $V_G - V_T$ for 7.5 nm, 10 nm (as in Fig. 4.6) 15 nm and 20 nm channel length devices, with channel widths and oxide thicknesses scaled accordingly. For this figure (and the following) for each device and method of calculation, we have somewhat arbitrarily defined the gate threshold voltage V_T as the voltage at which the drive current reaches 0.1 mA/µm. Thus, the ratios are unity at threshold by definition.

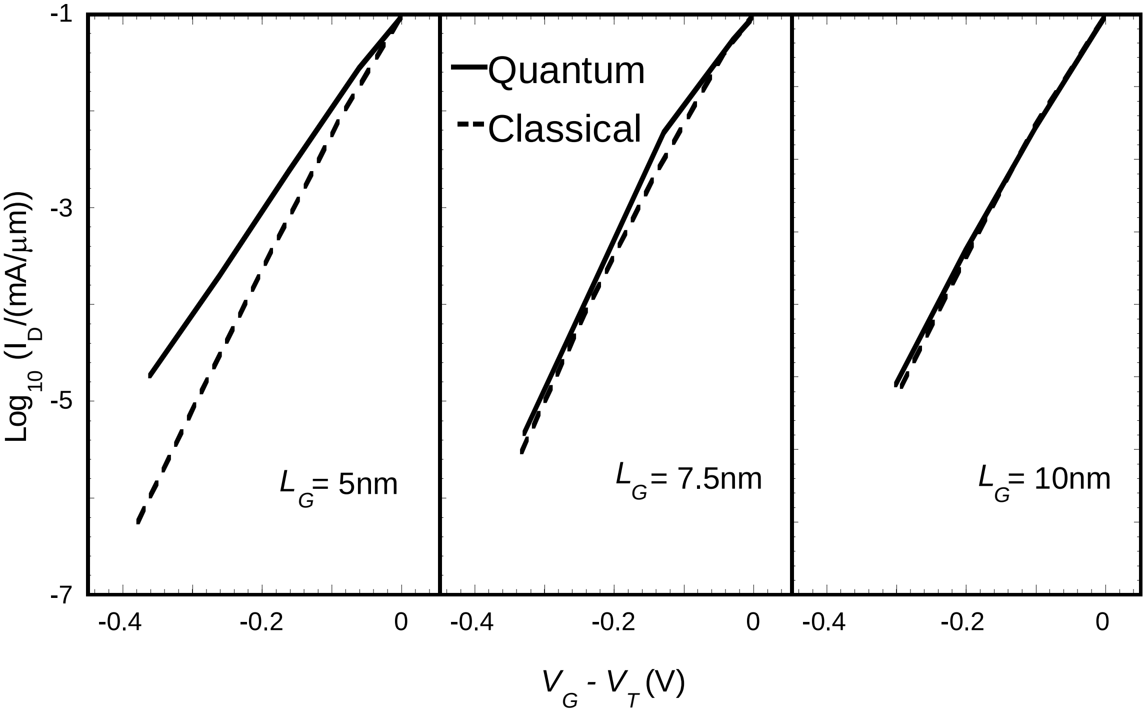

Figure 4.8: Subthreshold characteristics for the 7.5 nm and 10 nm devices of Fig 4.7 with well-behaved subthreshold characteristics by semiclassical or quantum analysis, and for a 5 nm device not otherwise considered here with unacceptable subthreshold characteristics due to source-to-drain tunneling. As for Figs. 4.7 we have defined the gate threshold voltage V_T as the voltage at which the drive current reaches 0.1 mA/µm.

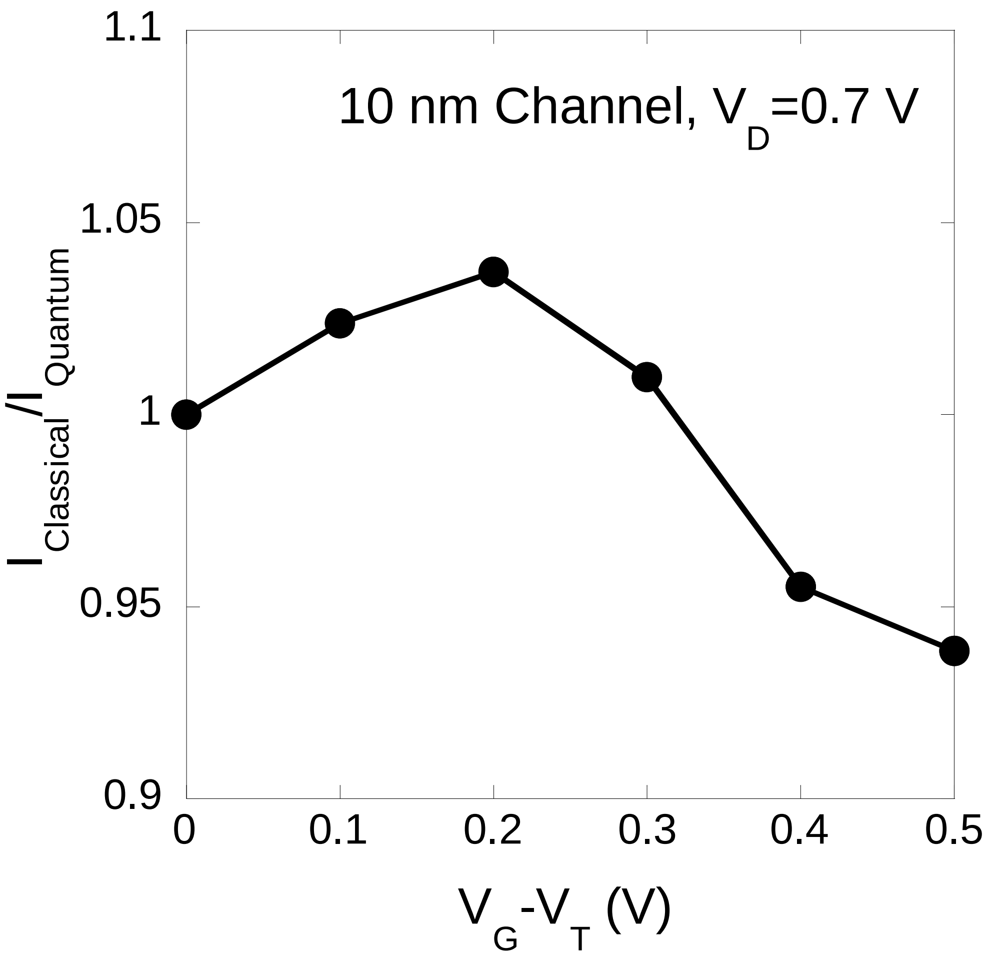
10 nm Channel, V_D=0.7 V
$I_{Classical}/I_{Quantum}$
1.1
1.05
1
0.95
0.9
0
0.1
0.2
0.3
0.4
0.5
V_G-V_T (V)

Fig. 4.9(a)

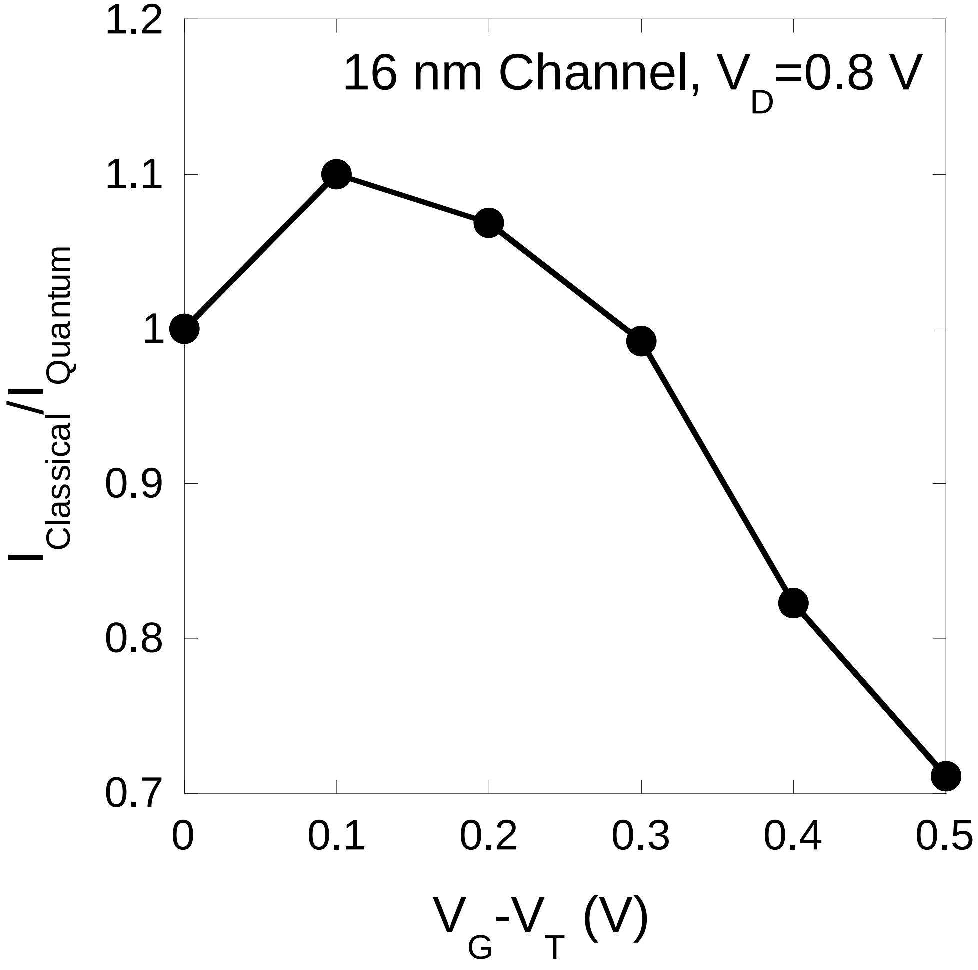

16 nm Channel, V_D=0.8 V
$I_{Classical}/I_{Quantum}$
1.2
1.1
1
0.9
0.8
0.7
0
0.1
0.2
0.3
0.4
0.5
V_G-V_T (V)

Fig. 4.9(b)

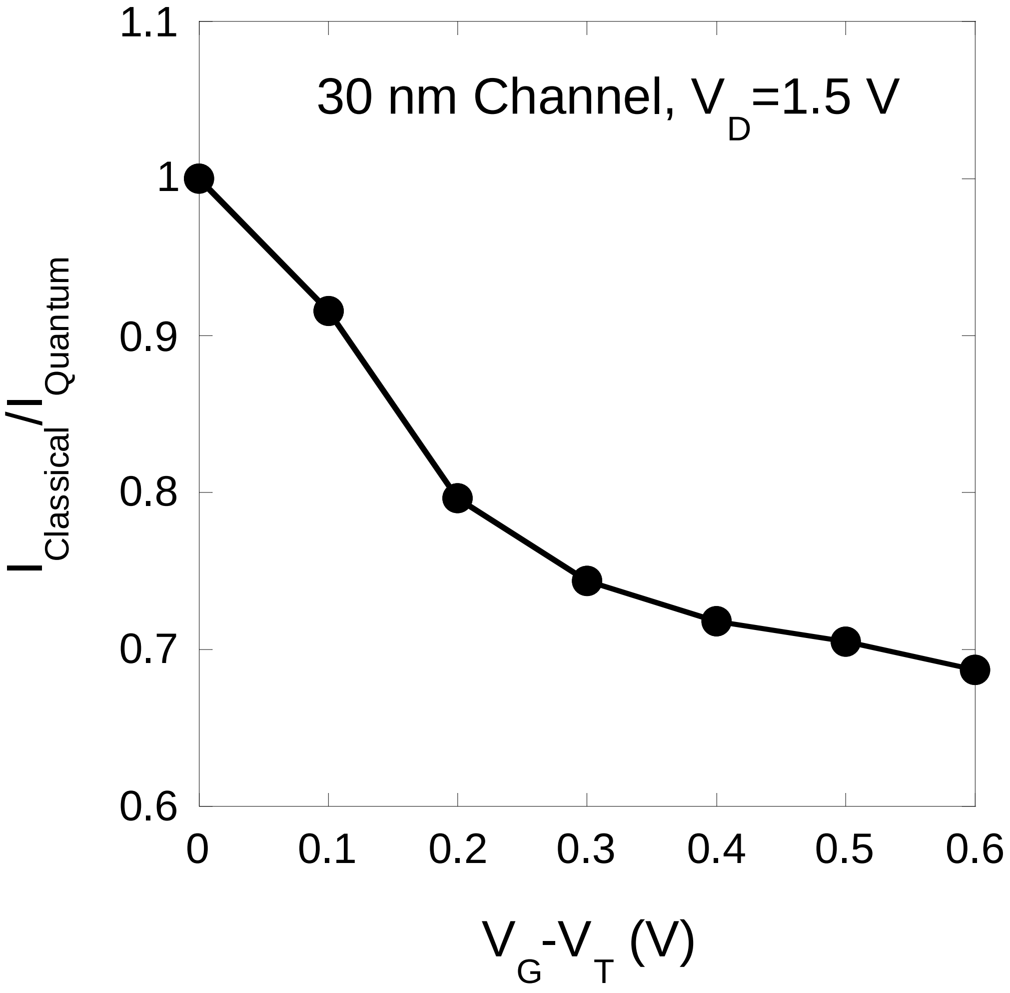

Fig. 4.9(c)

Figure 4.9: Ratios of semiclassically to quantum mechanically calculated current as a function of gate overdrive voltage $V_G - V_T$ for 10 nm, 16 nm and 30 nm channel length devices, with channel widths and oxide thicknesses again scaled accordingly for the larger devices. This time, however, the drain voltages were increased as to 0.7 V, 0.8 V and 1.5 V, respectively. As for Figs. 4.7 and 4.8, we have defined the gate threshold voltage V_T as the voltage at which the drive current reaches 0.1 mA/µm.

These variations between semi-classical and quantum transport simulations are not huge in absolute terms. However, to put these changes in perspective, note that, + within the approximations of Ref. [53], a 50% increase in channel mobility would produce only a 20% shift in the drive current. As we scale toward the nano-scale and more closely approach the ballistic limit, any changes to the ballistic limit, itself, become more important. Furthermore, we point out that in experiments (or simulations with scattering considered where this work began [64] before we stepped back to check the limiting behavior) these deviations in the ballistic limit of drive current from semi-classical expectations could be wrongfully attributed to changes in the scattering-mediated injection efficiency γ of Eq. (4.2), which may also exist but which are an, at least, nominally separate consideration. (And we remind the reader that we do not address to the well-known effects of quantum confinement normal to the transport direction in this work which were incorporated in both the quantum transport and "semi-classical" transport models here.) Of course, we emphasize that we have not attempted to explore all possible device geometries, doping distributions, materials and strain options, so we do not mean to claim that the behaviors seen here are universal, merely possible.

4.5 CONCLUSION

In summary, a comparison between semi-classically and quantum mechanically calculated above threshold ballistic charge injection velocities and drive currents in nano-scale double-gate MOSFETs has been performed. The well-know effects of quantum confinement were considered in both cases in an identical manner, only the treatment in the transport direction is varied. A substantial gate voltage dependence in the "thermal velocity" of injected carriers in nano-scale MOSFETs was observed, altering it from and even allowing it to exceed its semi-classically obtained value. Despite an opposing tendency of the drain current — increases in thermal velocity are accompanied by decreases in carrier density and vice versa — the result can be perhaps significant deviations from semiclassical expectations of the above threshold I_D-V_G, even while subthreshold characteristics remain well behaved. This work also illustrates that prediction of drive current, ballistic or perhaps otherwise, via separate predictions of the velocity and of charge density at the source-to-channel barrier top may be less quantitatively reliable at the nanoscale. Finally, we note that in experiments deviations in the ballistic limit of drive current from semi-classical expectations could be incorrectly attributed to changes in the scattering-mediated injection efficiency, which may also exist but which represents a separate issue.

CHAPTER 5. QUANTUM TRANSPORT IN DOUBLE GATE MOSFETs: EFFECT OF QUANTUM NONLOCALITY ALONG THE CHANNEL ON SCATTERING

5.1 INTRODUCTION

As pointed out in [63], the importance of scattering, as well as the accurate modeling of scattering, can not be neglected for the predictive simulation of transport even in 10 nm channel length MOSFETs, and likely below. In addition, as the universal mobility curve shows [64], different scattering mechanisms dominate in different effective (normal) field regimes. At low effective fields, impurity scattering dominates in conventional devices. When the effective field increases, the charge density and screening increase, thus reduces the impurity scattering. Phonon scattering then dominates (and increases due to quantum confinement) until, at still higher effective fields, surface roughness scattering dominates as the carriers propagate very close to the oxide-silicon interface.

As has been long established, quantum mechanical confinement can significantly affect carrier scattering rates [65]. However, as for ballistic transport, non-local quantum mechanical effects along the channel can affect the scattering rate as well. And the carrier's scattering rate (or perhaps more accurately, its imaginary self energy) as a function of position is affected not just by the quantum nature of the initial state but also by the quantum mechanical nature of the of final states and even self-consistent changes in both due to scattering. For non-randomizing processes, the degree of quantum mechanical non-locality can become more pronounced as we know from prior SEMC-based work [6]. For Si-based MOSFETs surface-roughness scattering is such a source of non-randomizing scattering.

5.2 SIMULATION METHODS

The implementation of phonon and surface scatterings is described in [11]. In this work, we consider how the scatterings along the channel changes when the channeling length changes.

Starting with a self-consistently calculated potential for a well-tempered Dual-Gate NMOSFET, as shown in Fig. 4.1, with channel length of 10nm, we artificially stretch the potential to form channel lengths of 20nm, 40nm and 80nm. To provide points of comparison, those potential profiles have exactly the same shape with respect to normalized position, as shown in Fig. 5.1, but the channel length varies relative to the wave lengths of the carriers so that the larger the channel length the more closely we approach classical behavior. Meanwhile, the potential transverse to the propagation direction and, thus, the effects of quantum confinement on scattering are held constant for the same normalized position along the channel. Average scattering rates as a function of normalized position were then calculated for each device for a thermal distribution of injected carriers weighted by the ballistic probability density as a function of normalized position and by the ballistic transmission probability for the 10 nm device (because we do not want the length of the channel and the total amount of scattering to affect the distribution of carriers considered and because we are not interested in the scattering of carriers that would not have been transmitted even without scattering). In this way the differences among the scattering rates at the same normalized position along the channel can only be attributed to non-local quantum mechanical effects along the channel.

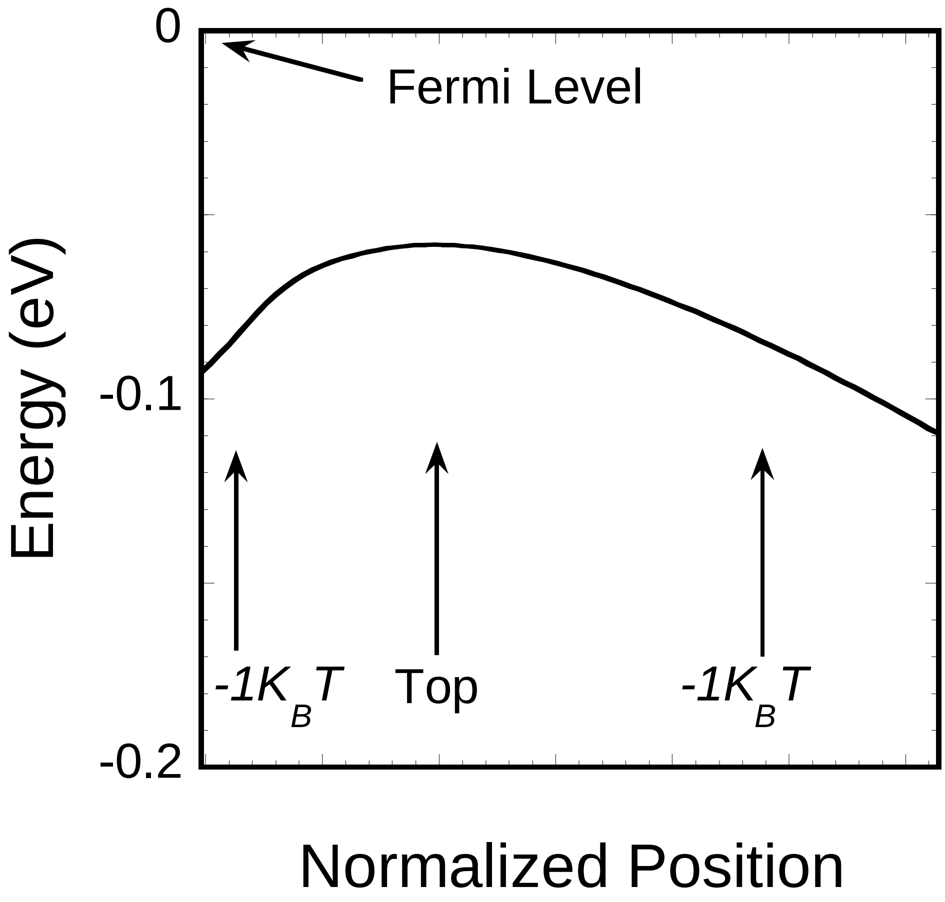

Figure 5.1: The first subband profile along the channel in the vicinity of the source-to-channel barrier top. Arrows indicate points at which the profile drops by $1k_BT$ from its peak.

5.3 RESULTS AND DISCUSSIONS

For randomizing phonon scattering, as shown in Fig. 5.2(a), the scattering rates (proportional to imaginary self energies) for thermally injected carriers change as a function of normalized position due to quantum mechanical variations in the density of states at and near the source-to-channel barrier top. For surface roughness scattering, as shown in Fig. 5.2(b), the effect is further complicated by the non-randomizing effectively long-range interaction potential. Note that the region where the potential drops by approximately k_BT beyond the barrier top is thought to be the most critical for determining channel injection efficiency. Within this region and beyond the scattering rate varies significantly due to the non-local quantum mechanical effects along the channel of thermal injected carriers shown in Fig. 5.1. In addition, a comparison to "quasi-semi-classical" results is provided in Fig. 5.3. The "semi-classical" result was obtained for long simulation regions width fixed subband energies defined by the local subband profiles for the 10 nm nMOSFET at the shown discrete points along the channel, and then weighted as before. Combined these results indicated that, while these non-local effects on scattering are small for 80 nm channel lengths, they quickly increase in size as the channel length decreases. Notably at the barrier top, and for surface roughness scattering which become dominant for narrow wells, the results for 20 nm channel lengths—where we are scheduled to be by the year 2009 according to the ITRS—are comparable to those for 10 nm channel lengths.

However, to say that scattering increases is not necessarily to say that current decreases. The latter depends on where the carriers go after scattering. Therefore the proportions of currents going through or reflected back from the channel with or without scattering for different channel lengths were calculated; results are provided in Table 5.1.

Again, the potential profile shape defined by the self-consistent results of Fig 5.1 for the 10 nm device was maintained as a control, and then the profile was stretched according to desired channel length. Critically for the calculations, as the channel length was increased, the coupling strength was turned down proportionally so that in a semiclassical calculation there would have been no difference in transmission probabilities with channel length. (Note that the net transmission probabilities due not correspond to what is commonly referred to as "injection efficiencies" as they are for all carrier incident in the leads, corresponding to a total incident current of 4,828 μA/μm as indicated in parentheses in Table 5.1, not just those that make it to the barrier top.) As the channel length was increased, the coupling strength was turned down proportionally so that in a semiclassical calculation there would have been no difference in transmission probabilities with channel length. Note that "without (w/o) scattering here means the transmission probability without having emitted or absorbed a phonon even though coupling was present. The results for the "ballistic" transport calculations with no scattering turned on are also shown for reference. While the drain current in the ballistic limit increased by 30% as the device size decreases from 80 nm to 10 nm, the drain current calculated with scattering increased by 53% despite the increased local scattering rates exhibited in Figs. 5.2 and 5.3. The greater relative increase in current with scattering is largely due to a 72% increases in the current flow associated with carrier that have scattered. Although it would be difficult to quantify in these quantum transport calculation, qualitatively speaking, it appears that the increases scattering rates are associated with strong coupling to final states significantly localized to the drain side of the source-channel barrier. In the meantime, the relative increase in the current of carriers that do not scatter, 32%, is approximately the same as that the current increase in the ballistic limit, 30%.

The above results suggest at least the possibility that as channel lengths decrease, the effects of scattering may actually become somewhat less significant than would be expected via semiclassical treatments of transport and scattering in the channel direction, this despite and overall increase in the scattering rate. For the results of Table 5.1, only the 10 nm device showed strong differences. However, its is noted that the scaled 20 nm, 40 nm and 80 nm devices are not necessarily representative of true devices of those gate lengths; such effects on scattering may occur for real device of large scale just as the effects for ballistic transport were more significant when self-consistent calculations of larger devices with larger drain voltages were performed.

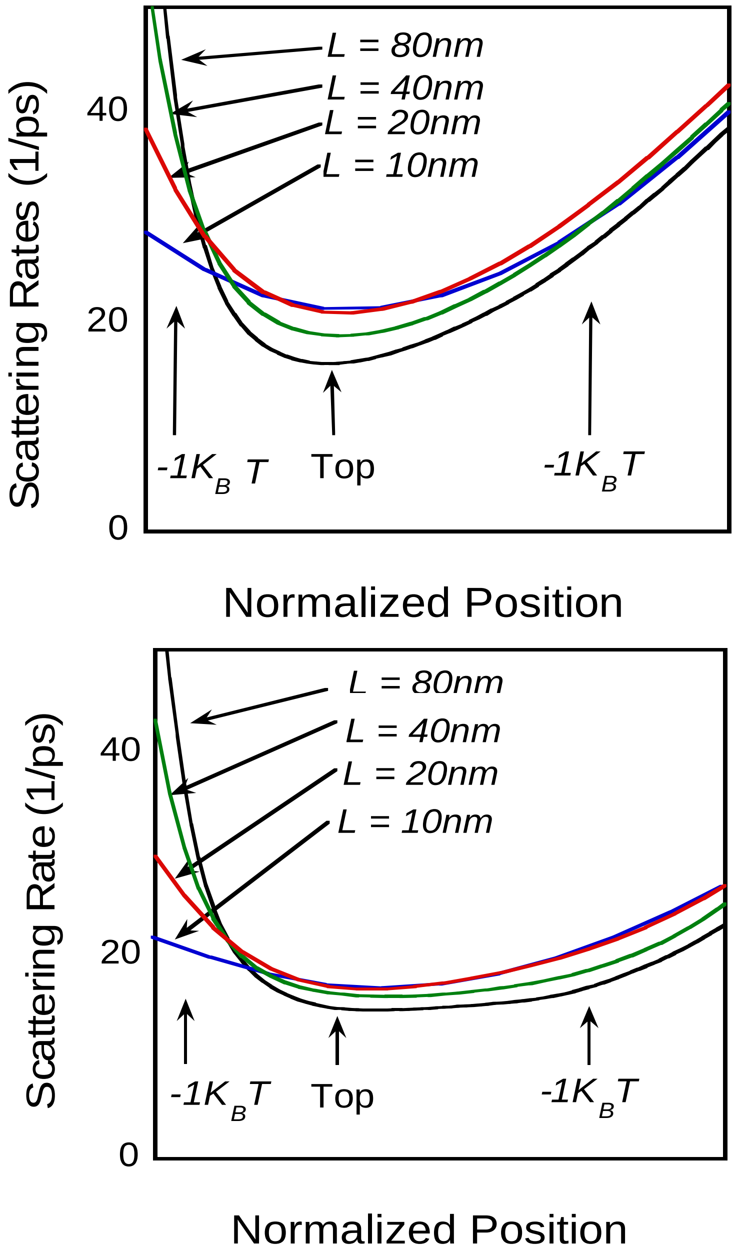

Figure 5.2: The average scattering rates near the barrier top for different channel lengths. (a) all types of phonon scatterings, (b) surface roughness scatterings.

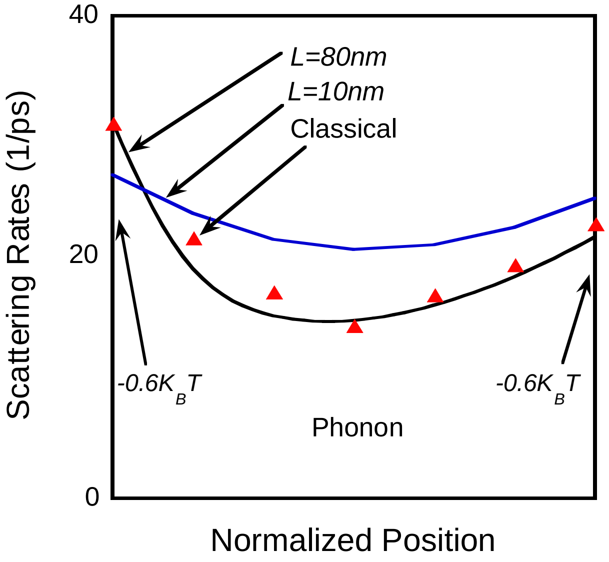

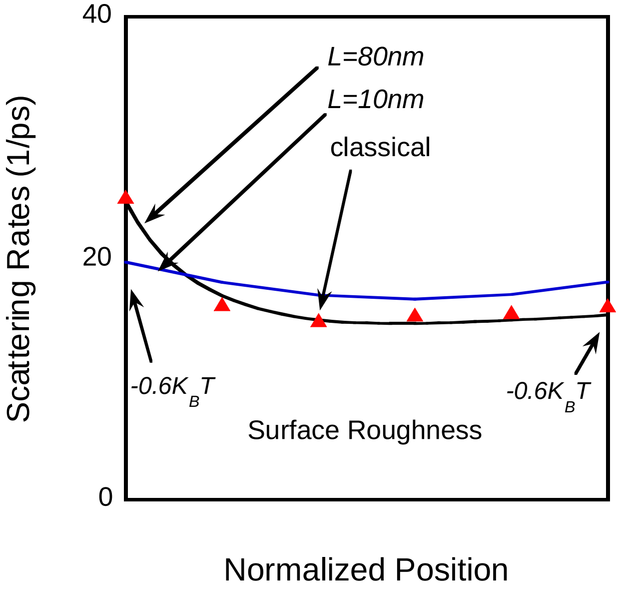

Figure 5.3: Quasi-classical calculation of scattering rates vs. those for 10 nm and 80 nm results of Fig. 5.2

	Transmission w/o scattering	Transmission after scattering	Reflection w/o scattering	Reflection after scattering
10nm (4828)	12.3% (595)	17.5% (844)	15.3% (739)	56.6% (2732)
Ballistic (4828)	57% (2745)	(0)	43% (2083)	(0)
20nm (4828)	9.9% (476)	11.8% (569)	17.2% (832)	59.0% (2846)
Ballistic (4828)	47% (2260)	(0)	53% (2567)	(0)
40nm (4828)	9.2% (445)	10.4% (500)	20.9% (1009)	58.3% (2814)
Ballistic (4828)	44% (2135)	(0)	56% (2692)	(0)
80nm (4828)	9.3%(451)	10.2%(491)	21.6%(1042)	59.9%(2890)
Ballistic (4828)	44% (2139)	(0)	56% (2688)	(0)

Table 5.1: Currents transmitted and reflected with and without (w/o) scattering. Numbers in brackets are currents in μA/μm. Ballistic results with scattering turned off are shown for comparison.

5.4 CONCLUSIONS

Nano-scale MOSFETs can exhibit significant non-local quantum mechanical effects on scattering along the channel (in addition to the well known effects on scattering of quantum confinement transverse to the channel). These non-local effects on scattering can be traced to the non-locality of the initial and final state density matrices, and also depends on the nature of the interaction. In our simulations, significant increases in scattering rates were found in the critical region in the vicinity of the barrier top. Despite this increased scattering rate the drive current also increased as compare to what would be expected semi-classically, even beyond the increase for ballistic transport, as the fraction of carrier transmitted after scattering increased. Together with the result of Chapter 4, this work illustrates that there can be significant quantitative limitations of semiclassical transport models no matter how physically accurate otherwise. (We, however, do not mean to imply that quantum transport simulations to date don’t have there own limitation.)

CHAPTER 6. SUMMARY AND RECOMMENDATIONS FOR FUTURE WORK

Previous chapters have covered in detail the development of polar optical phonon scattering mechanism in SEMC and its application in tunnel injection quantum well lasers. The ballistic transport and scattering effects in Si MOSFETs are also explored in depth. This Chapter summarizes the results of this work and discusses recommendations for future work.

6.1 SUMMARY AND CONCLUSIONS

The quantum transport simulator “Schrödinger Equation Monte Carlo” (SEMC) provides a physically rigorous treatment of quantum transport and phase-breaking inelastic scattering (in 3D) via real (actual) scattering processes such as optical and acoustic phonon scattering. It address the transition from quantum to semi-classical transport by solving the Schrödinger equation for a model coupled carrier-phonon transport many-body system, so that phase-breaking with respect to the carrier due to inelastic scattering occurs within SEMC just as it occurs within the true coupled system, via the change of the phonon coordinate. Thus, SMEC provides a rigorous foundation for study not only the quantum transport phenomenon but also the transition from semiclassical to quantum mechanical transport.

A (Quasi) one-dimensional (1D) version of SEMC (SEMC-1D) has been used to model the transition in nano-scale devices in order to gauge the potential reliability of semiclassical models, phase-coherent quantum transport, and other limiting models through the transition from semiclassical to quantum transport.

The work began with the injection and scattering in a tunnel injection laser structure in the presence of coupling to bulk phonon modes. This work demonstrates breakdown of Golden Rule based scattering calculations.

Then transport and scattering in quantum cascade lasers are studied. For this work I began by replacing the model bulk phonon modes with the confined and interface polar optical phonon modes of the heterostructure system for more realistic modeling of scattering, optical phonon mediated depopulation of intermediate states being an essential mechanism of operation for these devices. The calculation of these modes by transfer matrix method and the implementation of these modes into SEMC is the first challenge of this work. SEMC was then applied to simulate transport and scattering in a model quantum cascade laser, obtain results again not available via a Golden Rule treatment of scattering or, under some circumstances, in contradiction to expectations of a Golden Rule treatment of scattering.

Transport and scattering in Si-based nano-scale dual-gate MOSFET structures was then studied. I looked first at specific effects of quantum-mechanical non-locality along the channel on thermal velocity and drive current in the ballistic limits as channels shrinks toward and below 10 nm in length. It should be noted that this work was required to allow the isolation of the effects of quantum-mechanical non-locality along the channel on scattering in subsequent work. However, these limiting results were, nevertheless, of interest in themselves.

Finally the effects on scattering of non-local quantum mechanical effects along the channel were, themselves, studied. In self-consistent calculations of scattering, the carrier's scattering rate (or perhaps more accurately, it's imaginary self energy) as a function of position is affected not just by the quantum nature of the initial state but by the quantum mechanical density of final states. For non-randomizing processes, the degree of quantum mechanical non-locality can become more pronounced as we know from past work. For Si-based MOSFETs surface-roughness scattering is such a source of non-randomizing scattering.

6.2 RECOMMENDATION OF FUTURE WORK

6.2.1 Type-II Intersubband Laser

LO phonon-assisted interband tunneling in type-II intersubband laser heterostructures [69-72] is more efficient for the fast depopulation of the lower lasing states than the corresponding intersubband process in type-I double quantum wells (DQW). The main peak of the electron-phonon resonance in type-II DQW corresponds to electron transitions from the lowest electron-like subband to the top of the highest heavy-hole subband, which is strongly spin-split and displaced from the center of the Brillion zone due to the heterostructure asymmetry. Phonon-assisted depopulation can be conveniently employed even when the lower lasing level is designed near the upper edge of the heterostructure leaky window, where direct interband tunneling depopulation becomes inefficient. This design is beneficial for the laser performance providing the highest value of the matrix element for intrawell optical lasing transition and simultaneously preventing thermal backfilling of the lower lasing states.

6.2.2 Computational Efficiency

While Monte Carlo techniques are used to overcome computational limitations of direct solution method, the calculations still remain intrinsically computationally intensive themselves. Many efforts have been made to improve the computational efficiency. We shall discuss some of the techniques which may be helpful for optimizations.

Firstly, parallel computing is well-known to Monte Carlo simulation. In our case, particles injected into the devices are simulated independently. It is practical to distribute particles into different processors or machines by using multi-thread technology. Then we collect results from all the threads to generate the final report. The time cost of the coding of the parallel computing should be acceptable compared to the computational burden on single process.

Secondly, quasi-Monte Carlo [73-77] is based on the low-discrepancy sequences. This is in contrast to a regular Monte Carlo method, which is based on sequences of pseudorandom numbers. The accuracy of the quasi-Monto Carlo method increases faster than that of the Monte Carlo method with the same number of points. The random number generation in this quasi-Monte Carlo method, called low-discrepancy sequences or quasi-random number generation, have a definite pattern that fills in gaps evenly, qualitatively speaking. This method could reduce the number of particles we must inject into devices significantly.

6.2.3 Meshing and finite element method

The device geometry shows that the potential, carrier density, scattering rates and many other quantities are changing more rapidly around interfaces than deep in the body. So it is intuitively to see that finite element method (FEM) would be more appropriate than finite difference method (FDM), which we are currently using.

Other than the precision variability over the device that FEM offers, we can also handle more geometrically complicate devices by using FEM. FEM can provide more stable, precise, and efficient calculation than FDM. However there are issues with application of FEM methods to solving Schrödinger’s equation and associated NEFG equations. And the cost-benefit ratio must be considered for such a constantly evolving research code as SEMC.

6.2.4 The simulation of III-V Dual-Gate MOSFETs

Although III-V semiconductors have become an enabling progress technology in wireless and fiber optic communications and in quantum cascade lasers, CMOS has remained a Si-based technology. However, MOSFETs with gate lengths of a few 10's of nm are in production. SiO_2 gate oxide thickness is reaching a fundamental limit of approximately 1.5 to 1.0 nm, where quantum mechanical tunneling through the gate degrades transistor performs unacceptably. The simple scaling down of devices will not be sufficient to improve device performance in the future. As a result, the semiconductor industry is now considering so-called "non-classical" CMOS. Although the term "non-classical" is not a reference to quantum mechanics but simply to the use of non-conventional device designs and materials, quantum transport may well be required to fully understand their behavior as per the example of the ultra-thin-body dual gate devise considered above. The use of high-κ gate dielectrics is a well know example of a potential non-classical CMOS technology. However, coulomb scattering from charge trapping and the phonon issue related to the high-κ gate dielectrics have resulted in degraded channel mobility. The need for continuing improvement in device performance has also lead to the research on strained Si, Si-Ge alloys and Ge for obtaining higher mobility [66-68].

There is also now (or once again) an interest in using III-V semiconductors. III-V such as GaAs, InSb have much higher electron mobilities, and, thus, offer, improved device performance, at least for n-channel devices [16-18], although the reduced density of states in these devices can be counterproductive. Also bandgap engineering and direct bandgaps, not available in Si- and Ge-based material systems, allow for the possibility of novel designs and high performance integrated optoelectronic circuits combining MOS and photonic devices. However, with longer electron wavelengths, longer phase coherence lengths and scattering often dominated by non-randomizing polar optical phonon scattering, consideration of quantum transport becomes even more critical.

In many respects consideration of electron transport in III-V is simpler from a quantum transport simulation point of view. Consideration of only one spherical conduction band minima for at least low energy carriers is such an example. However, fundamental to physics of transport in III-Vs is the long-range polar-optical phonon interactions. The challenge of the simulation is to practically implement those long-range scattering mechanism into the program. While, in fact, the original 1-D version of SEMC was actually designed to specifically address this problem, it still provides a much greater challenge than consideration of randomizing deformation scattering. For now we shall consider bulk modes only, as in case of deformation potential scattering Si previously [11], which should be sufficient to understand the essential physics of transport and scattering in these devices.

Similar to 1D, the 2D correlation function of for polar optical phonon scattering has the approximate form:

$$\begin{aligned}
&\left\langle M(x)M^{+}(x')\right\rangle = \\
&\sum_{q}^{Q}\int dydz\int dy'dz'(\varphi^{+}(x,y,z)M_{q}(x,y,z)\varphi(x,y,z))(\varphi^{+}(x',y',z')M_{q}(x',y',z')\varphi(x',y',z')) \\
&= C\int dydzdy'dz'\varphi^{+}(x,y,z)\varphi(x,y,z)\varphi^{+}(x',y',z')\varphi(x',y',z')e^{i\Delta k\bullet\Delta z}\int dq(\frac{e^{iq\Delta r}}{q^{2}}) \\
&= C\int dydzdy'\varphi^{+}\varphi\varphi^{+}{}'\varphi'(\int dz'e^{i(\Delta k-q_{z})\Delta z})\int dq_{x}dq_{y}(\frac{e^{iq_{x}\Delta x}e^{iq_{y}\Delta y}}{q_{x}^{2}+q_{y}^{2}+q_{z}^{2}}) \\
&= C\int dydzdy'\varphi^{+}\varphi\varphi^{+}{}'\varphi'\int dq_{x}dq_{y}(\frac{e^{iq_{x}\Delta x}e^{iq_{y}\Delta y}}{q_{x}^{2}+q_{y}^{2}+\Delta k_{z}^{2}}) \\
&= C\int dydzdy'\varphi^{+}\varphi\varphi^{+}{}'\varphi'\int_{0}^{2\pi}d\theta\cdot e^{iq_{r}\cos\theta\cdot\Delta r}\int_{0}^{\infty}dq_{r}\cdot q_{r}\cdot\frac{1}{q_{r}^{2}+\Delta k_{z}^{2}} \\
&= 2\pi C\int dydzdy'\varphi^{+}\varphi\varphi^{+}{}'\varphi'\int_{0}^{\infty}J_{0}(q_{r}\Delta r)\cdot\frac{q_{r}}{q_{r}^{2}+\Delta k_{z}^{2}} \\
&= 2\pi CK_{0}(\Delta k_{z}\Delta r)
\end{aligned}$$

Where J_0 is the Bessel function of the first and K_0 is the Hankel function.

And the coupling potential is

$$P(r)\propto\int_{-\infty}^{\infty}e^{iq_{r}\Delta r}\,\frac{1}{(q_{r}^{2}+\Delta k_{z}^{2})^{\frac{1}{4}}}dq_{r}=\left|\frac{r}{2\Delta k_{z}}\right|^{\frac{1}{4}}\cdot\frac{\Gamma(\frac{1}{2})}{\Gamma(\frac{1}{4})}\cdot K_{-\frac{1}{4}}(\Delta k_{z}r)$$

The implementation of this polar optical phonon scattering into SEMC-2D should be analogous to the surface roughness scattering in SEMC-2D for Silicon, whose coupling potential is also a Hankel function. [11]

BIBLIOGRAPHY

1. R. H. Dennard, F. H. Gaensslen, H.-N. Yu, V. L. Rideout, E. Bassous, and A. R. LeBlanc, "Design of ion-implanted MOSFET's with very small physical dimensions," *IEEE Journal of Solid-State Circuits*, vol. sc-9, pp. 256-268, 1974.

2. International Techanology Roadmap for Semiconductors 2005 Edition, Executive Summary, pg 5 (http://www.itrs.net/Links/2005ITRS/Home2005.htm).

3. D. K. Ferry, R. Akis, and D. Vasileska, "Quantum effects in MOSFETs: use of an effective potential in 3D Monte Carlo simulation of ultra-short channel devices," in *Technical Digest. IEDM*, 2000, 287-290.

4. Z. Ren, R. Venugopal, S. Datta, M. Lundstrom, D. Jovanovic, and J. Fossum, "The ballistic nanotransistor: a simulation study," in *Technical Digest. IEDM*, 2000, 715-718.

5. M. V. Fischetti, "Master-equation approach to the study of electronic transport in small semiconductor devices," *Physical Review B* (Condensed Matter), vol. 59, pp. 4901-4917, 1999.

6. L. F. Register, "Schrodinger equation Monte Carlo: bridging the gap from quantum to classical transport," in *Quantum-Based Electronic Devices and Systems*, vol. 14, Selected Topic in Electronics and Systems, M. Dutta and M. A. Stroscio, Eds.: World Scientific, Singapore, 1998, pp. 251-279, and in *Int. J. high-Speed Electronics and Systems*, vol. 9, 251 (1998);

7. L. F. Register and K. Hess, "Simulation of carrier capture in semiconductor quantum wells: bridging the gap from quantum to classical transport," *Applied Physics Letters*, vol. 71, pp. 1222-1224, 1997.

8. W. Chen, X. Zheng, M. Stroscio, and L. F. Register, "Quantum transport simulation of carrier transport and energy relaxation with tunnel injection lasers," in 8th International Workshop on Computational Electronics (IWCE-8), 2001.

9. W. Chen, L. F. Register, and S. K. Banerjee, "Simulation of quantum effects along the channel of ultrascaled Si-based MOSFETs," *IEEE Transactions on Electron Devices*, vol. 49, pp. 652-657, 2002.

10. W. Chen, L. F. Register, S. K. Banerjee, "Two-dimensional quantum mechanical simulation of electron transport in nano-scaled Si-based MOSFETs", *Physica E*, vol. 19, pp. 28-32, 2003.

11. W. Chen, L. F. Register, S. K. Banerjee, "Schrodinger Equation Monte Carlo-2D for Simulation of Nanoscale MOSFETs", In reviewed at *IEEE Transactions on Electron Devices*.

12. W. Chen, "Schrodinger equation Monte Carlo simulation of Nano-scaled semiconductor devices", Ph. D. Thesis, University of Texas at Austin, 2004 (http://wwwlib.umi.com/cr/utexas/fullcit?p3150561)

13. M. A. Stroscio, M. Kisin, G. Belenky, and S. Luryi, "Phonon enhanced inverse population in asymmetric double quantum wells", *Applied Physics Letters*, vol. 75, pp. 3258-3260, 1999.

14. X. Zheng, W. Chen, M. Stroscio, and L. F. Register, "Nonequillibrium Green's function analysis of inter-well transport and scattering in monopolar lasers". *Physical Review B (Condensed Matter)*, vol. 73, 245304, 2006.

15. X. Zheng, W. Chen, L. F. Register and S. K. Banerjee, "Anomalous injection velocities in short channel double-gate MOSFETs". Reviewed by *IEEE Transactions on Electron Devices*.

16. Y. L. Huang, P. Chang, Z.-K. Yang, Y.-J. Lee, H.-Y. Lee, H.-J.Lie, J. Kwo, J. P. Mannaerts, M. Hong, "Thermodynamic stability of Ga2O3(Gd2O3)/GaAs interface", *Applied Physics Letters*, vol. 86, No. 191905, 2005.

17. S. Datta, T. Ashley, J. Brask, L. Buckle, M. Doczy, M. Emeny, D. Hayes, K. Hilton, R. Jefferies, T. Martin, T.J. Phillips, D. Wallis, P. Wilding, R. Chau, "85nm gate length enhancement and depletion mode InSb quantum well transistors for ultra high speed and very low power digital logic applications", *IEEE IEDM*, 2005.

18. M. Passlack, R. Droopad, K. Rajagopalan, J. Abrokwah, R. Gregory, D. Nguyen, "High mobility NMOSFET structure with high-k-dielectric", *IEEE Transactions on Electron Devices*, vol. 26, pp. 713-715, 2005.

19. K. Ismail, "Si/SiGe high-speed field-effect transistors," in *Technical Digest. IEDM*, 1995, 509-512.

20. L. F. Register and K. Hess, "Numerical-simulation of electron-transport in mesoscopic structure with weak dissipation", *Physical Review B (Condensed Matter)* vol. 49, pp. 1900-1907, 1994.

21. R. P. Feynman, Statistical Mechanics: A set of Lectures, Addison-Wesley, 1972, p.226.

22. L. F. Register, “Schrpdinger equation Monte Carlo: bridging the gap from quantum to classical transport”, *International Journal of High Speed Electronics and Systems*, Vol. 9, No. 1, pp. 251-279, 1998.

23. P. Bhattacharya, “Tunnel injection Lasers”, *International Journal of High Speed Electronics and Systems*, Vol. 9, pp. 847-866, 1998.

24. M. Grupen and K. Hess. “Severe gain suppression due to dynamic carrier heating in quantum well lasers”, *Applied Physics Letters*, vol. 70, pp. 808-810, 1997.

25. M. Grupen and K. Hess. “Simulation of Carrier Transport and nonlinearities in quantum-well Laser diodes”, *IEEE Journal of Quantum Electronics*, vol. 34, pp. 120-140, 1998.

26. S. Yu, K. W. Kim, M. A. Stroscio, G. J. Iafrate, J. P. Sun, and G. I. Haddad, “Transfer matrix method for interface optical-phonon modes in multiple interface heterostructure systems”, *Journal of Applied Physics*, vol. 82, pp. 3363-3367, 1997

27. J. Faist, F. Capasso, D. L. Sivco, C. Sirtori, A. L. Hutchingson, and A. Y. Cho, “Quantum cascade laser”, *Science*, vol. 264, pp. 553-536, 1994.

28. X. Zhang, G. I. Haddad, J. P. Sun, A. Afzali-Kushaa, C. Y. Sung, and T. Norris, “Population inversion in step quantum wells at 10μm wavelength”, in 1995, 53rd Annual Device Research Conference Digest, p.118-119.

29. C. Y. Sung, T. B. Norris, A. Afzali-Kushaa, and G. I. Haddad, “Femtosecond intersubband relaxation and population inversion in stepped quantum well”, *Apply physics Letters*, vol. 68, pp. 435-437, 1996.

30. X. Zhang, C. Y. Sung, T. B. Norris, and G. Haddad, “Population inversion in asymmetrical step quantum wells and infrared intersubband lasers”, *Proc. SPIE* vol. 2694, pp. 19-27, 1996.

31. A. Lucas, E. Kartheuser, and R. G. Bardo, “Electron –phonon interaction in dielectric films. Application to electron energy loss and gain spectra”, Physical Review B (Condensed Matter). vol. 2, pp. 2488-2499, 1970.

32. J. J. Licari and R. Evrard. “Electron-phonon interaction in a dielectric slab: effect of the electronic polarizability”, *Physical Review B* (Condensed Matter). vol. 15, pp. 2254-64, 1977.

33. R. Fuchs and K. L. Kliewer, “Optical modes of vibration in an ionic crystal slab”, Phys. Rev. vol. 140, pp. A2076-A2088, 1965. “Optical modes of vibration in an ionic crystal slab including retardation. I. Non-radiative region”, *Physical Review*, vol. 144, pp. 495-503. 1966.

34. N. Mori and T. Ando, “Electron-optical-phonon interaction in single and double heterostructures”, *Physical Review B* (Condensed Matter), vol. 40. pp. 6175-6188, 1989.

35. D.Y. Oberli, J. Shah, T. C. Damen, J. M. Kuo, and J. E. Henry, J. Lary, S. M. Goodnick, “Optical phonon-assisted tunneling in double quantum well structures”, *Applied Physics Letters*, vol. 56, pp. 1239-1241, 1990.

36. J. Faist, F. Capasso, C. Sirtori, D.L. Sivco, A. L. Hutchinson, M. S. Hybertsen, and A.Y. Cho, “Quantum cascade lasers without intersubband population inversion”, *Physical Review Letters*, vol. 76, pp. 411-414, 1996.

37. R. Kohler, R.C. Iotti, A Tredicucci, F Rossi, “Design and simulation of terahertz quantum cascade lasers”, *Applied Physics Letters*, vol. 79, pp. 3920-3922, 2001.

38. R. Kohler, A. Tredicucci, F. Beltram, H.E. Beere, E.H. Linfield, A.G. Davies, D.A. Ritchie, R.C. Iotti,; F. Rossi, “Terahertz semiconductor-heterostructure laser”, *Nature*, vol. 417, pp. 156-159, 2002.

39. B. Williams, S. Kumar, H. Callebaut, Q. Hu, J. L. Reno, “Terahertz quantum-cascade lasers operating up to 137K”, *Applied Physics Letters*, vol. 83, pp. 5142-5144, 2003.

40. H. Callebaut, S. Kumar, B. Williams, Q. Hu, J. L. Reno, “Analysis of transport properties of tetrahertz quantum cascade lasers”, *Applied Physics Letters*, vol. 83, pp. 207-209, 2003.

41. B. Williams, S. Kumar, H. Callebaut, Q. Hu, J. L. Reno, “3.4-THz quantum cascade laser based on longitudinal-optical-phonon scattering for depopulation”, *Applied Physics Letters*, vol. 82, pp. 1015-1017, 2003.

42. R. Kohler, A. Tredicucci, C. Mauro, F. Beltram, H.E. Beere, E.H. Linfield, A.G. Davies, D.A. Ritchie, “Terahertz quantum-cascade lasers based on an interlaced photon-phonon cascade”, *Applied Physics Letters*, vol. 84, pp. 1266-1268, 2004.

43. H. Callebaut, S. Kumar, B. Williams, Q. Hu, J. Reno, “Importance of electron-impurity scattering for electron transport in terahertz quantum-cascade lasers”, *Applied Physics Letters*, vol. 84, pp. 645-647, 2004.

44. H. Teng, J.P. Sun, G.I. Haddad, M.A. Stroscio, S. Yu, K.W. Kim, “Phonon assisted intersubband transitions in step quantum well structures”, *Journal of Applied Physics*, vol. 84, pp. 2155-2164, 1998.

45. S.-F. Huang, C.-Y. Lin, Y.-S. Huang, T. Schafbauer, M. Eller, Y.-C. Cheng, S.-M. Cheng, S. Sportouch, W. Jin, N. Rovedo, A. Grassman, Y. Huang, J. Brighten, C. H. Liu, B.Von Ehrenwell, N. Chen, J. Chen, O. S. Park, M. Commons, A.

Thomas, M.-T. Lee, S. Rauch, L. Clevenger, E. Kaltalioglu, P. Leung, J. Chen, T. Schiml, and C. Wann, “High performance 50nm CMOS devices for microprocessor and embedded processor core applications”, *Technical Digest. IEDM*, pp11.1.1-4, 2001.

46. Y. Taur, D. A. Buchanan, W. Chen, D. J. Frank, K. E. Ismail, S. H. Lo, G. A. Sai-Halasz, R. G. Viswanathan, H.-J. C. Wann, S. J. Wind, and H.-S. Wong, “CMOS scaling into the nanometer regime”, *Proceedings of the IEEE*, vol. 85, pp. 486-504, 1997.

47. L. Chang, Y.-k, Choi, D. Ha, P. Ranade, S. Xiong, J. Bokor, C. Hu, and T. J. King, “Extremely scaled silicon nano-CMOS devices”, *Proceedings of the IEEE*, vol. 91, pp. 1860-1873, 2003.

48. V. Chan, R. Rengarajan, N. Rovedo, W. Jin , T. Hook, P. Nguyen, J. Chen, E. Nowak, X.-D. Chen, D. Lea, A. Chakravarti, V. Ku, S. Yang, A. Steegen, C. Baiocco, P. Shafer, H. Ng, S.-f. Huang, and C. Wann, “High speed 45nm gate length CMOSFETs integrated into a 90nm bulk technology incorporating strain engineering”, *Technical Digist. IEDM*, pp. 318-314, 2003.

49. T. Tanaka, K. Suzuki, H. Horie, T. Sugii, “Ultrafast operation of V_{th}-adjusted P^+-n^+ double-gate SOI MOSFETs”, *IEEE Electron Device Letters*, Vol. 15, pp. 386-388, 1994.

50. H.-s. P. Wong, K. K. Chan, and Y. Taur, “Self-aligned (top and bottom) double-gate MOSFET with a 25nm thick silicon channel”, in *Technical Digest. IEDM.* New York, NY, USA: IEEE, 1997, pp. 427-430.

51. D. J. Frank, S. E. Laux, and M. V. Fischetti, “Monte Carlo simulation of a 30nm dual-gate MOSFET: how short can Si go?”, in *Technical Digest. IEDM*, 1992, pp, 5530556.

52. K. Natori, “Ballistic metal-oxide-semiconductor field effect transistor”, *Journal of Applied Physics*, vol. 76, pp. 4879-4890, 1994.

53. M. Lundstrom, “Elementary scattering theory of the Si MOSFET”, *IEEE Electron Device Letters*, vol. 18, pp. 361-363, 1997.

54. K. Natori, “Scaling limit of the MOS transistor”, *IEICE Transactions on Electron Devices*, vol. E84-C, pp. 1029-1036, 2001.

55. T.-S. Xia, L. F. Register and S. K. Banerjee, “Quantum Transport in Double-Gate MOSFETs with Complex Bandstructure,” *IEEE Transactions on Electron Devices*, vol. 50, pp. 1511-1516, 2003.

56. J.-H. Rhew, M. S. Lundstrom, “Drift-diffusion equation for ballistic transport in nanoscale metal-oxide-semiconductor field effect transistors”, *Journal of Applied Physics*, Vol. 92, pp. 5196-5202, 2002.

57. M. S. Lundstrom, Z. Ren, “Essential physics of carrier transport in nanoscale MOSFETs”, *IEEE Transactions on Electron Devices*, vol. 49, pp. 133-141, 2002.

58. J.-H. Rhew, Z. Ren, M. S. Lundstrom, “A numerical study of ballistic transport in a nanoscale MOSFET”, *Solid-State Electronics*, vol. 46, pp. 1899-1906, 2002

59. A. Rahman, J. Guo, S. Datta, M. S. Lundstrom, “Theory of ballistic nanotransistors”, *IEEE Transactions on Electron Devices*, vol. 50, pp. 1853-1864, 2003.

60. F. Assad, Z. Ren, D. Vasileska, S. Datta, M. S. Lundstrom, “On the performance limits for Si MOSFET’s: a theorycal study”, *IEEE Transactions on Electron Devices*, vol. 47, pp. 232-240, 2000

61. Z. Ren, R. Venugopal, S. Goasguen, S. Datta, M. S. Lundstrom, “nanoMos 2.5: a two-dimensional simulator for quantum transport in double-gate MOSFETs”, *IEEE Transactions on Electron Devices*, vol. 50, pp. 1914-1925, 2003.

62. International Techanology Roadmap for Semiconductors 2005 Edition, Executive Summary, pg 57 (http://www.itrs.net/Links/2005ITRS/Home2005.htm).

63. W. Chen, L. F. Register, and S. K. Banerjee, “Simulation of quantum and scattering effects along the channel of ultra-scaled Si-based MOSFETs”, *Proc. Device Research Conf.*, pp. 109-110, 2002

64. S. Takagi, M. Iwase, and A. Toriumi, “On the universality of inversion-layer mobility in n- and p-channel MOSFETs”, *Technical Digest. IEDM*, vol. 8, pp.398-401, 1988.

65. S. Yamakawa, H. Ueno, K. Taniguchi, C. Hamaguchi, K. Miyatsuji, K. Masaki, U. Ravaioli, “Study of interface roughness dependence of electron mobility in Si inversion layers using the Monte Carlo method”, *Journal of Applied Physics*, vol. 79, pp. 911-916 (1996).

66. R. Oberhuber, G. Zandler, P. Vogl, “Subband structure and mobility of two-dimensional holes in strained Si/SiGe MOSFET's”, *Physical Review B (Condensed Matter)*, vol.58, pp. 9941-9948, 1998

67. M.V. Fischetti, Z. Ren, P.M. Solomon, M. Yang, K. Rim, “Six-band k·p calculation of the hole mobility in silicon inversion layers: dependence on surface orientation, strain, and silicon thickness”, *Journal of Applied Physics*, vol. 94, pp. 1079-95, 2003.

68. E.X. Wang, P. Matagne, L. Shifren, B. Obradovic, R. Kotlyar, S. Cea, M. Stettler, M.D Giles, “Physics of hole transport in strained silicon MOSFET inversion layers”, *IEEE Transactions on Electron Devices*, vol.53, pp. 1840-1851, 2006

69. H. Ohno, L. Esaki, E.E. Mendez, “Optoelectronic devices based on type-II polytype tunnel heterostructures”, *Applied Physics Letters*, vol.60, pp. 3153-3155, 1992

70. K. Ohtani, H. Ohno, “Intersubband electroluminescence in InAs/GaSb/AlSb type-II cascade structures”, *Applied Physics Letters*, vol.74, pp. 1409-1411, 1999

71. R.Q. Yang, “Mid-infrared interband cascade lasers based on type-II heterostructures”, *Microelectronics Journal*, vol.30, pp. 1043-1056, 1999

72. M.V. Kisin, M.A. Stroscio, S. Luryi, G. Belenky, “Interband tunneling depopulation in type-II InAs/GaSb cascade laser heterostructure”, *Physica E*, vol.10, pp. 576-586, 2001

73. H.G. Niederreiter, “Quasi-Monte Carlo methods and pseudo-random numbers”, *American Math. Society*, vol.84, pp. 957-1041, 1978

74. H.G. Niederreiter, “Random Number Generation and Quasi-Monte Carlo Methods”, *Society for Industrial and Applied Mathematics*, 1992. ISBN 0-89871-295-5

75. J.M. William, E.C. Russel, “Quasi-random sequences and their discrepancies”, *Journal of Scientific Computing*, vol. 15, pp. 1251-1279, 1994

76. M. Drmota, R.F. Tichy, “Sequences, discrepancies and applications”, Lecture Notes in Math., 1651, *Springer*, Berlin, 1997, ISBN 3-540-62606-9

77. O. Strauch and Štefan Porubský, “Distribution of Sequences: A Sampler”, *Peter Lang Publishing House*, Frankfurt am Main 2005, ISBN 3-631-54013-2

VITA

Xin Zheng was born in Wuhan, Hubei, China on June 7, 1975, the son of Zhong Zheng and Jun Tian. After completing his work at Wuhan Foreign Language School, Wuhan, Hubei, in1990, he entered Wuhan Iron and Steel Company No. 3 Affiliate High School. After graduation, he entered Peking (Beijing) University in Beijing, China. He received Bachelor of Science Degree in Physics from Peking University in June, 1997. Then he worked as an instructor in Huazhong Agricultural University. After that, he was admitted to the Physics Department in the Iowa State University in September 1998. He transferred to the Electrical and Computer Engineering Department in University of Texas at Austin in September 2000. He received Master of Science Degree in Electrical Engineering in May 2003. He is currently working in Fore Research and Management as an associate analyst.

Permanent Address: 126 Street, Apt 84-2, Qingshan, Wuhan, Hubei, China 430081

This dissertation was typed by the author.